UNIVERSITY OF TWENTE.

Faculty of Electrical Engineering, Mathematics & Computer Science

Deterministic Modelling and Parameterization of Height-dependent Interaction between Radio waves and Human body

Meghashree Srikantaiah Manjesh
M.Sc. Electrical Engineering

Thesis Report
[September 2020]

Daily supervisor:
dr. Y. Miao

External supervisor:
dr.ir. H.S. Bindra

Committee chair:
dr. A. Alayón Glazunov
dr. ir. A.B.J. Kokkeler

Radio Systems
Faculty of Electrical Engineering,
Mathematics and Computer Science
University of Twente
P.O. Box 217
7500 AE Enschede

Acknowledgement

I would like to take this opportunity to acknowledge and thank all the people who have supported, guided, and kept me motivated throughout the journey.

My sincere gratitude to my daily supervisor dr. Y. Miao, for her patience, constant guidance, and motivation. I would like to thank dr. A. Alayón Glazunov and dr.ir. A.B.J. Kokkeler for their valuable inputs, support, and cooperation. I also would like to thank dr.ir. H.S. Bindra for evaluating my thesis at short notice. Many thanks to Nirmal and Suraj who played a major role during the measurement campaign. I would like to extend my thanks to Ram Narayanan and Jayanth for their timely help.

I especially thank my parents for their continuous support and encouragement, despite all the unforeseen difficulties. I also thank my friend Darshan for being a helping hand during the difficult times. I would like to remember my uncle Late Shashidhar Jayaram and dear grandfather Late Jayaram who has inspired me in many ways.

Lessons learned and knowledge gained both professionally and personally from every individual during this process is a valuable treasure.

Abstract

In an indoor wireless environment, the presence of the human bodies significantly influences the radio link between the access point and user equipment due to their low heights. It is essential to include human body models in the most widely used deterministic propagation models, wherein the human body has to be approximated to certain geometry and associated electromagnetic properties. The circular conducting/dielectric cylinder is the most widely used geometrical approximation for the standing posture of the human body. By visual inspection, the human body form does not appear to be symmetric and uniform at different heights, unlike cylinders. Furthermore, the dielectric nature of the human body may cause frequency-dependent human-radio interaction. Therefore comparative measurement and deterministic modelling of human-radio interaction at sub-6GHz and higher frequencies considering the accountability of cylinder simplification at different height is the main goal of this project. The frequencies of choice, one at mid-band sub-6 GHz and one at high-band close to 20 GHz, are representative in the current development of 5G. This work re-evaluates the accountability of using cylinder geometry at both sub-6GHz and higher frequencies.

Contents

List of Figures

List of Tables

1 Introduction

1.1 Background

The diversity of indoor wireless applications has increased considerably in recent years. The performance of the indoor wireless systems is significantly influenced by the radio propagation environment, the frequency bands, and the resulting multipath channel. The multipath propagation channel is a result of the interaction of electromagnetic waves with surrounding objects. Similarly, the presence of the human bodies may cause scattering of electromagnetic waves, when the dimension of the human body becomes relatively larger than the dimension of wavelength resulting in significant changes in the signal strength, time, and phase. For this reason, the effects and characterization of human body scattering on radio links at different frequency bands for various applications have been investigated by several studies [1][2][3]. The studies are done under various experimental setups in an indoor environment. For example a human body at different positions with respect to the transmitter and the receiver within the measurement environment, a human body at different positions with respect to the Line of Sight(LoS) link, a human body crossing the LoS link, channel variations due to the human body movement in the indoor environment, shadowing effects due to the different orientation of the human body, etc.

Deterministic channel models based on ray tracing and geometric optics techniques take into consideration the geometrical and electromagnetic properties of the interacting objects(IOs). Therefore in such propagation models, human bodies are approximated by a certain geometry based on the morphology and associated electromagnetic properties. The computational electromagnetic wave techniques such as Method of Moments(MoM) [4], Finite-Difference Time-Domain(FDTD) method [1], Physical optics(PO) [5], Uniform Theory of Diffraction(UTD) [6] etc are used to estimate the physical mechanism of the human-radio interaction.

The most widely used geometrical model for the standing posture of the human body is the conducting/dielectric circular cylinder [6]. The simplest model is one cylinder approximating the whole body and the improvised models have each body part, ex: legs, arms, torso, etc. approximated by cylinders of different radius [7]. As we know the human body is not exactly cylindrical when observed from different angles around the human body. Therefore in deterministic modelling it is vital to consider a cylinder model with a radius that best fits from all observation angles around the human body. Furthermore, the dielectric nature of the human body may cause frequency-dependent human-radio interaction. Therefore the objective of this thesis is measuring and comparative deterministic modelling of height-dependent human-radio interaction taking account of cylinder simplification of the human body. Considering recent advancement in 5G technology, the frequencies at Mid-band sub-6GHz and close to High-band is chosen for comparative modelling. This work re-evaluates the accountability of using cylinder simplification at both sub-6GHz and higher frequencies.

1.2 Literature Review

Indoor wireless channel communication is strongly influenced by human bodies in contrast to the outdoor systems because the transmission power and the height of the base stations are much lower. It is observed that the presence of the human body results in significant changes in the channel gain [1]. Over the last few decades the study of the propagation characteristics of radio waves in the presence of the human body has increased at higher frequencies, e.g. Mid-band sub-6GHz, High-band, mmWave frequencies, etc. due to the recent development of 5G and mmWave technologies.

The human body has a complex shape consisting of different layers of tissues each with its permittivity and conductivity. Therefore Electromagnetic(EM) wave can be transmitted through, absorbed by, and reflected in varying degrees, depending on the tissue properties, morphology, and frequency. In deterministic channel propagation models, various human body models have been used to estimate the attenuation due to human body scattering or blockage. The developed models differ based on the posture dependent geometrical approximation, frequency-dependent dielectric property, and on the mathematical model used to estimate the EM interaction. The geometrical model can be either two or three dimensional based on the requirements. In the case of 2D, it can be modelled as a disk, ellipse, rectangular thin film, etc whereas in the case of 3D it can be modelled as a parallelepiped, ellipsoid, spheroid, cylinder, etc. The kind of material constituting these geometrical models can be a perfect conductor, lossy dielectric, or absorber which will influence the electromagnetic phenomenon associated with the model.

In [8], a comparison between ten human body models that differ in shape, material, and computational techniques used with the ray-tracing algorithm was made. The general implementation scheme of the models was presented and the results were compared with the empirical data, obtained through a 2.4GHz transmission while a single human body was crossing the LoS. The absorbing cylindrical human body model was chosen as the most appropriate for the human body shadowing analysis when the human body crosses the LoS. However, the case where the human body is in the ray vicinity, without intercepting LoS is not explored in this research.

In [3], to study the effect of the movement of the human body close to LoS link a measurement scenario was setup in which a metallic circular cylinder was used as a human body approximation. The transmitter and receiver are in fixed positions and the cylinder is moved in parallel to the LoS link. The experiment is conducted at 10GHz, the simulation and measurement results are compared and showed that the human motion affects LoS link for close distances. In [6], the same experimental setup as previously has been used. Continuous-wave experimental measurements are done using a cylinder approximated as a human body torso with a radius of 0.25m. The effect of the reflected ray in the channel as a function of the cylinder radius in the range 0.15 to 0.35m is investigated. It is observed in their experiment that the influence of radius is more in the vicinity of the transmitter/receiver antennas.

Plouhinec et al in [9] has developed a 3D UTD modeling of a measured antenna disturbed by a finite length dielectric circular cylinder for WBAN applications. The model is validated with the measurement results of an antenna disturbed by a cylindrical phantom which is a cylindrical plastic bottle filled with MSL1800 phantom liquid. The measurement was done at 4.5GHz and 3GHz. The presented model gives results very close to measurement results.

In [4], scattering by the lossy dielectric elliptical cylinder and the elliptical cylinder with circular cylinders which is approximated as the human body is examined. MoM numerical technique was used for theoretical analysis. The dielectric values are referred from the literature[10] wherein permittivity and conductivity of human body samples are measured. It is observed that for front incidence, the relative power at the elliptical cylinder back is smaller than in other cases. This means that the cross-section of the elliptical cylinder shadow at the observation plane affects the absorption of the incident power. The frequency characteristics of the equivalent diameter of an elliptical cylinder to model the human body are also studied in this literature. For the lower frequencies, the equivalent diameter is larger than that of higher frequency. This hypothesis is justified by comparing the numerical results with the experimental results at 3.35GHz.

In [4], it is studied that when the human bodies are close to each other it cannot be treated independently as there could be mutual interference and the absorption of an electromagnetic wave by human bodies are not independent. MoM technique is used to investigate the scattering by two independent dielectric cylinders at 3.35GHz wherein dielectric and conductivity values are taken from the literature [10]. These cylinders are modelled as a person. The cylinders are placed adjacently with varying distances between them in two different co-ordinate axis such as x and y-axis. It is also proven that the scattering by two independent cylinders touching each other is the same as the scattering by the equivalent circumscribed cylinder with twice the radius.

There have been studies on the human body effect at High-band frequencies. In [11], the attenuation caused by the human body is investigated at 26GHz and 39GHz. Different human body models such as the Knife Edge(KE) model, UTD single-cylinder model, double cylinder model representing 2 arms of the human body are used to compare with the measured human attenuation. It is found that the KE model is concise, simple, and better predicts the attenuation if the shape of the model representing the human body is neglected. The double cylinder UTD model overestimates the attenuation. The attenuation and the penetration loss is generally higher at 39GHz than 26GHz. A dynamic channel model for moving human bodies in an indoor channel environment is proposed by Michael et al [12]. The Thalmann human walking model with 12 body parts modelled as a dielectric cylinder of different radii except for the head which is modelled as a sphere is developed. The transmitter and receiver are set at two different heights to study the effects of the upper body(torso and arms) and the lower body(legs). The time-dependent body part translations and rotations are used with ray tracing and UTD calculations to characterize the time-varying channel conditions. The human body crosses the Line of Sight (LoS) transmission link at these two heights. The measurement is done at 2.4GHz and 31.8GHz. At 2.4GHz the simulation results are compared with the measurement results and also with the simple model consisting of only one cylinder. The simulation results of the developed model show good agreement with the measurement results but when compared with the single-cylinder model the difference is high for the lower body parts than the upper body level. The analysis at 31.8 GHz shows that there is a difference in the simulation results of the two models.

Compared to Mid-band and High-band frequencies human body blockage is prominent at mmWave frequencies as the human body becomes electrically large. In [13], the experimental results show that there can be greater than 40dB shadowing loss at 57 to 64GHz mmWave frequencies when the human body blocks the LoS path completely. In [14], the human body is geometrically approximated as the infinitesimally thin absorbing screen. KE mathematical model is used for numerical analysis. The applicability limits and feasibility of using such a simple diffraction model to compute the blocking of the human body at millimeter-wave radio frequencies in indoor environments is the main goal of this research.

In [15], a deterministic indoor radio propagation channel is modelled in the presence of a human to investigate the path loss statistics at 60GHz mmWave frequency. The human body is considered as a perfectly conducting circular cylinder. The analysis is done in different indoor environments. Statistical parameters were obtained for different room sizes to study the effects of an increasing number of persons on the distribution of the received signal strength. The variance of the path loss increased non linearly as the number of persons increased for fixed room size. For a fixed number of persons, increasing the room size resulted in a decreased variance of the path loss. The effects of varying the room dimensions for a given area and a different number of persons were also investigated.

Due to increasing interests in mmWave communications, Ting Wu et al[16] provides examples of the global regulatory requirements for mmWave exposure of the human body for 60GHz. Also, the propagation characteristics of mmWaves in the presence of the human body are studied, and the thermal effects due to the mmWave radiation on the body were also evaluated using 4 different models: naked skin, naked forehead, clothed skin, hat on the forehead. Their simulation results show that the lowest steady-state temperature elevation is produced in the naked skin model since the heat generated in the skin can be dissipated and taken away by the blood flow in the muscle whereas the highest steady-state temperature elevation is produced in the hat on the forehead model since the skin is covered with the cloth. The dependence of clothing thickness upon the power transmission coefficient and steady-state temperature elevation was also studied using the clothed skin model. Their simulation results also predict that about 34% to 42% of the power is reflected by the skin surface at 60GHz.

The frequency-dependent complex permittivity should be determined when the human body is approximated as the dielectric material. Gabriel et al[17], has done a literature survey on the dielectric properties of tissues and presented in a graphical format by extracting data from different literature. The data are presented in a graphical format to highlight the information concerning the frequency coverage and the scatter in the data. They made a basis for their research[18] based on the existing gap in the available knowledge. In [18], the dielectric properties of the different tissues and parts of the human body(also animals) are measured using the VNA, impedance analyzers, and open-ended coaxial probes which are used to interface the measuring equipment. Measurement was done on human autopsy material after 24 to 48hours after death. The dielectric parameters were found for the frequency range 10MHz - 20GHz. In [19], a proof of concept to measure the dielectric properties of internal body components(lung, heart, etc) and to effectively determine irregularities in real-time is presented based on the simulation. A surgery-free method is proposed for an on-body monitoring system to evaluate the dielectric properties by using a set of electrodes at low frequencies (10MHz) to obtain data that can determine the underlying layered structure. The permittivity and conductivity values obtained in the latter and similar kinds of literatures are used in cases where human body is assumed as the dielectric cylinders.

1.3 Problem Statement

From the literature review, cylindrical human body models are extensively used to study the scattering and shadowing caused by the human body. Mostly, this approximation is used in the scenario where the human body obstructs the LoS or is located in the close vicinity of the LoS. Human body scattering is studied in a scenario where both transmitting and receiving antennas are in fixed positions meaning that scattering is observed from only a part of the human body at only one incidence angle of source. There is a lack of study on the human body scattering observed from different angles around it with different incidence angles of source considering cylinder simplification. Although the cylinder models are studied at various frequencies there is a lack of comparative deterministic modelling at different frequencies.

- With the recent advancement of 5G for indoor applications, the High-band spectrum (typically in the range of 24GHz to 40GHz) offers high data speed, capacity, quality, and low latency but the coverage is limited. For wider-area coverage, combination with mid-band(3.5GHz to 8GHz) is essential [20]. There is a lack of comparative deterministic modelling of the human body at High-band and Mid-band frequency bands considering the accountability of cylinder simplification.

- The human body dimension at a different angle around the human body and at different heights is different. Therefore in deterministic modelling it is vital to consider a cylinder model radius that best fits the human body at all the incidence angles of source around the body.

1.4 Objective

Measuring and comparative deterministic modelling of height-dependent human-radio interaction at Mid-band Sub-6GHz and higher frequency close to High-band. This motivates the selection of two frequency bands with 2GHz bandwidth centered at 3.6GHz, and 19GHz. Analyzing the scattering caused by the human body at different angles around it for a different incidence angle of the source is also part of the thesis. The morphology of the head, torso, and leg of the human body is different compared to the cylinder and hence this work re-evaluates the accountability of using cylinder geometry at these three heights.

The Uniform Theory of Diffraction (UTD) solution for a dielectric circular cylinder offers a relatively fast analyzing method and also provides a clear and valuable physical picture for the mechanisms of scattering via rays. It also provides a solution that is continuous across the surface shadow boundaries and is valid in the transition regions. Therefore UTD solution for a dielectric circular cylinder model is chosen for the simulation model as the human body has dielectric nature. The simulated Angular Power Spectrum is compared with the measured Angular Power Spectrum to evaluate the prediction accuracy of the model.

2 Modelling Methodology

In this section, details of the Uniform Theory of Diffraction for dielectric circular cylinder is discussed. It also includes the modelling technique used.

2.1 Physical Mechanism of Radio-Body Interaction

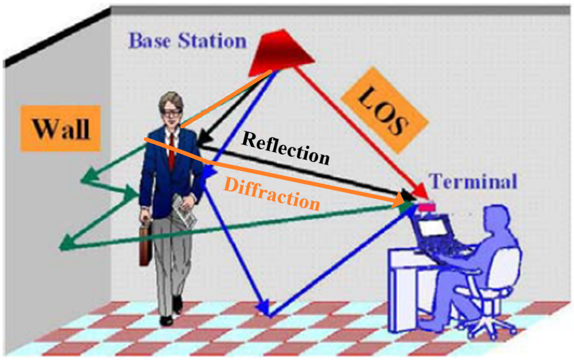

Figure 2.1: Radio-body interaction in an indoor environment. Image source:[3]

The study of radio propagation is vital in the design of practical radio systems. The radio waves that travel in a straight line from the transmitting antenna to the receiving antenna are referred to as LoS. Besides the LoS, other basic mechanisms governing the propagation of electromagnetic waves when the radio waves impinge on the human body are:

1. **Reflection**: Reflection occurs when the human body is larger than the wavelength of the impinging electromagnetic wave. There are two kinds of reflection: *Specular* & *Diffused*. If the standard deviation of the surface roughness is significantly smaller than the wavelength, incidence waves can still be seen as specularly reflected. Otherwise, the incidence wave is scattered into multiple directions due to the interaction with a rough surface. The same surface may be rough or smooth depending on the frequency of the impinging wave and the angle of incidence [21] [22].

2. **Refraction**: Refraction is the change in the direction of a wave passing from one medium to another or from a gradual change in the medium. As we know the human body is composed of various layers of tissues with its dielectric and conductive properties. Therefore refraction plays a major role in intra-body communication systems. [21]

3. **Diffraction**: Human body is closed and an impenetrable obstacle which means it can block the electromagnetic field causing shadowing. Due to Huygen's principle, secondary waves are formed even behind the human body, which leads to the existence of a diffracted field. Geometrical Theory of Diffraction and Uniform Theory of

Diffraction are used to calculate these diffracted fields in the shadow region. The human body may also experience surface diffracted rays.

4. **Absorption**: The absorption induced in the human body due to the exposure of the electromagnetic fields depends on the frequency and dielectric properties of the tissues. The absorption seems to be higher in the tissues of high water content such as muscle, brain tissues, internal organs ,and skin, while the absorption is lower in the tissues of low water content such as fat and bone [10].

At different frequencies, combinations of these phenomena are experienced at varying intensities. In this project, we mainly focus on calculating the scattering caused by the human body at Sub-6GHz and high frequency close to 20GHz therefore study of the refraction mechanism is not part of our analysis. In the following sections, a mathematical method used to calculate the scattering caused by the human body is explained.

2.2 High-Frequency Asymptotic Modeling of Radio-Body Interaction

The high-frequency phenomena mean that the fields being considered in a system where the properties of the medium and the size parameters of the scatterer vary little over an interval on the order of a wavelength [23]. When the number of unknowns to evaluate the scattered fields grows whenever the working frequency becomes higher, the full-wave methods, ex: Fast Multipole Method(FMM), Finite Element Method(FEM), MoM, FDTD, Finite-Difference Frequency-Domain(FDFD) cannot tackle the analysis of such problems beyond an upper limit determined by the computational requirements in terms of time and memory. High-frequency techniques consist in the asymptotic evaluation of Maxwell's equations [24]. As a consequence, they provide good accuracy when dealing with electrically large geometries meanwhile the computational needs diminish with respect to the aforementioned methods. This method does not have an intrinsic frequency limitation however it is restricted by the fact that the size of the scatterer must be large in terms of the wavelength at the given frequency.

Within the high-frequency techniques, the Geometrical Optics(GO) and the Physical Optics(PO) are the most extended methods due to the successful results obtained in various fields.

2.2.1 Physical Optics

In physical optics or wave optics, the propagation is in terms of waves. The physical optics approximation is a technique based on the determination of equivalent current densities induced on the surface of an illuminated plane. Once the equivalent current densities are obtained, both electric and magnetic field levels can be calculated from the corresponding radiation integrals. This model predicts the phenomena such as interference, diffraction, polarization, etc which are not explained by classic geometric optics [24].

2.2.2 Geometrical Optics

In Geometric Optics or ray optics, propagation is described in terms of rays wherein the ray is a model for the path taken by EM radiation emitted by a source. The main property of a ray is that of being a straight line and whose paths are governed by the laws of reflection and refraction at interfaces between different media. The failure of GO to predict the correct fields in the shadow regions is a serious shortcoming because EM fields have to be smooth and continuous everywhere, the discontinuities across the shadow boundaries cannot occur in nature. Nevertheless, ray tracing based GO is a powerful technique due to its unique simplicity and gives better physical insight. Therefore a cure for its failure is found instead of rejecting the method altogether. The Geometrical Theory of Diffraction (GTD) was developed by Keller in the 1950s as an extension of geometrical optics. By adding the diffracted rays Keller succeeded in correcting the deficiency in the GO that predicts zero fields in the shadow regions. However, the shortcoming of the GTD was that it was not uniform in the sense that it predicts the diffracted fields in regions away from the shadow boundaries, but became singular in the transition regions surrounding such boundaries. In 1974 Kouyoumjian and Pathak had succeeded in developing a ray-based Uniform Theory of Diffraction(UTD) that is valid everywhere in space. They had performed an asymptotic analysis and found that by multiplying the diffraction coefficients by a transition function, the diffracted fields remain bounded across the shadow boundaries. Because of its characteristics, UTD is usually preferred by researchers and practicing engineers for treating the EM scattering from the canonical geometries [23]. There are three different UTD curved-surface-diffraction solutions based on the location of the source and the observation points relative to the scattering object. It is classified as a scattering problem, the radiation problem ,and the coupling problem. The scattering problem, wherein both the source and the observation points are off the surface of the scattering object is relevant to this project.

2.3 Uniform Theory of Diffraction – A GO method

The Uniform Theory of Diffraction can be used to compute the total electric field associated with ray tracing. The geometrical configuration for the scattering problems of a smooth circular convex surface is illustrated in Figure 2.2. The extension of the incident ray beyond the point of grazing at Q_1 and Q_3 on the surface defines the Shadow Boundary(SB) which broadly divides the space exterior to the surface into the lit and the shadow regions. The UTD offers a solution for the field both in the lit and the shadow regions. S is the source point, P_L ,and P_{LS} is the observation point in the lit region and P_S is the observation point in the shadow region. The electric field represented in the vector form are: $\overrightarrow{SP_L}$ is the direct ray, $\overrightarrow{Q_rP_L}$ is the reflected ray, $\overrightarrow{Q_{2,4}P_s}$ is the diffracted ray. The total field in the lit region is the sum of direct and reflected fields. It may also include surface diffracted fields if the surface of the obstacle is closed, however, their field is generally negligible. In the shadow region, only diffracted rays exist.

Figure 2.3 illustrates the details of the geometry to calculate the reflected field. An $e^{j\omega t}$ time dependence is assumed and suppressed in the present analysis. ω and t refers to

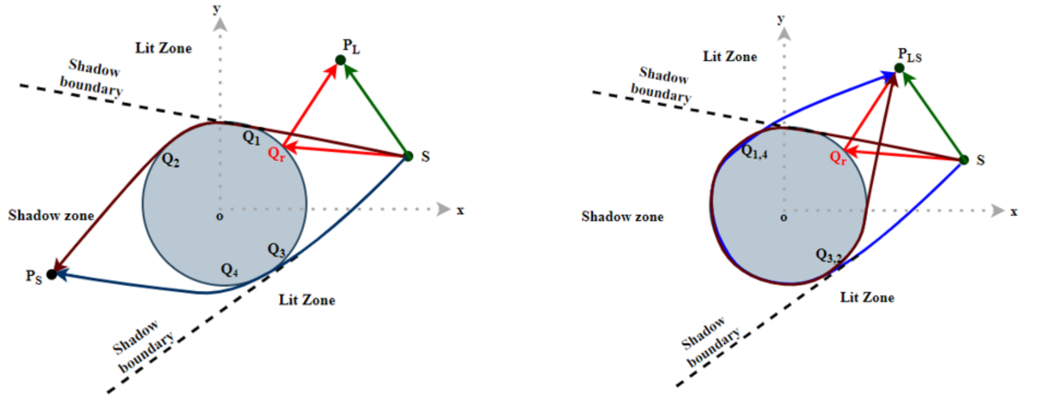

(a) Electric field components in lit and shadow region

(b) Surface diffracted field in the lit region for a closed object

Figure 2.2: General illustration of the scattering problems of a smooth circular convex surface.

angular frequency and time.

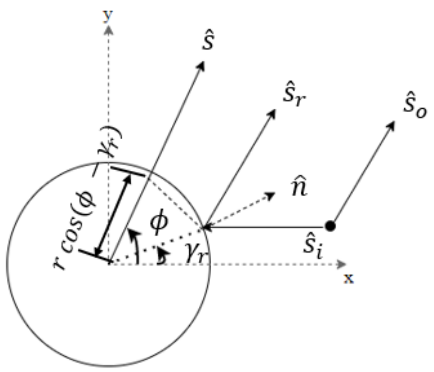

Figure 2.3: Geometrical details for the calculation of electric field in the lit region. Image source: [23]

Assuming that the observation point is in the far-field zone, the observation point can be referred by observation direction ϕ rather than observation point as such. The unit vector from the source point to the observation direction is denoted as $\hat{s}_o$ and the unit vector from the reflection point to the observation direction is denoted as $\hat{s}_r$, $\hat{s}$ is the vector at observation direction. The direct and reflected vectors can be given as:

$$\hat{s}_o = \hat{s}_r = cos(\phi)\hat{x} + sin(\phi)\hat{y} \tag{2.1}$$

The unit normal vector at the reflection point Q_r, which lies on the surface of the cylinder is given by:

$$\hat{n} = cos(\gamma_r)\hat{x} + sin(\gamma_r)\hat{y} \tag{2.2}$$

γ_r is the angle at which the reflection point is located. It is measured from the x-axis as shown in figure 2.3.

2.3.1 Direct Field

The expression for the direct field from the source point,S to the observation point,P_L as shown in figure 2.2 for a spherical wave incidence is given as:

$$E^i_{s,h}(\phi) = A_{directivity}\overrightarrow{E}_{s,h}\frac{e^{(-jks_o)}}{s_o} \tag{2.3}$$

where, $A_{directivity}$ is the approximation of the antenna directivity, $\overrightarrow{E}_{s,h}$ is the polarization vector, k is the wave number, s_o is the distance between the source and the observation point,P_L. The subscripts s and h are soft and hard components which is equivalent to the vertical and horizontal component respectively. Since the observation point is assumed to be at the far-field zone, the direct field notation is observation direction-dependent instead of the observation point. s_o on the L.H.S of equation 2.3 is the magnitude of the vector $\hat{s}_o$ which is direction-dependent as described previously.

The Jones vector formulation for the vertical polarization expressed in a circular basis is used which is expressed as:$1/\sqrt{2}[-1; 1]$. Antenna directivity, $A_{directivity}$ is calculated based on the comparison of the angle, θ between the incident field vector $\hat{s}_i$, and the direct field vector $\hat{s}_o$, with the beamwidth angle, θ_{BW} of the transmitting antenna at different receiver positions. The expression is:

$$A_{directivity} = \begin{cases} A_{max} - \dfrac{2}{0.5\theta_{BW}}\theta & \text{If } \theta \leq 0.5\ \theta_{BW} \\ 0 & \text{otherwise} \end{cases} \tag{2.4}$$

A_{max} is the maximum antenna gain on a linear scale. This approximation is taken as antenna pattern information was unavailable. The direct field is considered as the spherical wave field because the transmitting and the receiving antennas do not necessarily maintain the far-field distance from each other.

2.3.2 Reflected Field

At a far-field distance from the spherical wave source, the field components oriented in the incident direction, $\hat{s}_i$ usually have decayed so rapidly that the only significant components are those transverse to the $\hat{s}_i$ and are related in precisely the same way as those of a plane wave, therefore the field incident on the reflection point can be considered as locally plane. Hence it follows that the direction of the incident plane wave vector at the point of reflection Q_r is:

$$\hat{s}_i = -cos(\phi_i)\hat{x} - sin(\phi_i)\hat{y} \tag{2.5}$$

Special case: For the plane wave incidence at Q_r with an angle of incidence $\phi_i = 0°$, the incident ray unit vector can be given as:

$$\hat{s}_i = -\hat{x} \tag{2.6}$$

Locating the reflection point Q_r

Given the observation direction ϕ, we must find the associated reflection point Q_r. According to the law of reflection, the angle of incidence is equal to the angle of reflection which yields the expression:

$$-\hat{n} \cdot \hat{s}_i = \hat{n} \cdot \hat{s}_r \tag{2.7}$$

For each observation angle ϕ, this equation has to be solved for the angle γ_r to locate the point of reflection Q_r. γ_r is the angular variable that is associated with the reflection point.

Determination of the reflection caustic distance

At reflection point Q_r, we know that $cos(\theta^i) = \hat{n} \cdot \hat{s}_r$ therefore:

$$\theta^i = cos^{-1}(\hat{n} \cdot \hat{s}_r) \tag{2.8}$$

The reflected ray tube caustic distance ρ_r(i;e the radius of curvature of the reflected ray at its reference point Q_r) is obtained from the relation[25]:

$$\frac{1}{\rho^r} = \frac{1}{\rho^i(Q_r)} + \frac{2}{rcos(\theta^i)} \tag{2.9}$$

where ρ^i is the radius of the curvature of the incident wavefront at the point of reflection Q_r, r is the radius.

Incident field at reflection point

The incident field at Q_r with its phase referenced to the source position is

$$E^i_{s,h}(Q_r) = \overrightarrow{E}_{s,h}\frac{e^{-jks_i}}{s_i} \tag{2.10}$$

s_i is the distance between the source and the reflection point Q_r.

Reflected field at observation point

The reflected field in the direction ϕ is [25]:

$$E^r_{s,h}(\phi) = E^i_{s,h}(Q_r)\overline{\overline{R}}A_r e^{-jks_r} \tag{2.11}$$

A_r is the spreading factor of the reflected field expressed as:

$$A_r = \sqrt{\frac{\rho_r}{\rho_r + s_r}} \tag{2.12}$$

$\overline{\overline{R}}$ is the dyadic reflection coefficient which can be written as

$$\overline{\overline{R}} = R_s \hat{e}^i_\perp \hat{e}^r_\perp + R_h \hat{e}^i_\parallel \hat{e}^r_\parallel \tag{2.13}$$

$\hat{e}^{i,r}_\perp$ and $\hat{e}^{i,r}_\parallel$ are perpendicular and parallel unit vectors respectively of the incident and reflected electric fields. According to the ray-fixed coordinate system, these unit vectors are computed using the equations below [24]:

$$\hat{e}^{i,r}_\perp = \frac{\hat{s_{i,r}} \times \hat{n}}{\parallel \hat{s_{i,r}} \times \hat{n} \parallel} \tag{2.14}$$

$$\hat{e}^r_\parallel = \hat{e}^{i,r}_\perp \times \hat{s_{i,r}} \tag{2.15}$$

According to the law of reflection, the reflected ray lies in the plane of incidence, i.e. the one containing the incident ray and the normal to the surface at the reflection point, it follows that $\hat{e}^i_\perp = \hat{e}^r_\perp = \hat{e}_\perp$.

The UTD reflection coefficient is defined as [9]:

$$R_{s,h} = -\sqrt{\frac{-4}{\xi_L}} e^{-j\frac{(\xi_L)^3}{12}} G_{s,h}(\xi_L, X_L) \tag{2.16}$$

with:

$$\xi_L = -2m(Q_r)\cos\theta^i \qquad \& \qquad X_L = 2kL_L\cos^2\theta^i \tag{2.17}$$

X_L is the argument of the transition function. The transition function is the Fresnel integral which is explained later. ξ_L is the fock parameter associated with the reflected field.

Total electric field in the lit region

The total electric field in the lit region is the sum of the direct field and the reflected field given as:

$$E^{lit}_{s,h}(\phi) = E^i_{s,h}(\phi) + E^r_{s,h}(\phi) \tag{2.18}$$

2.3.3 Surface Diffracted Fields

Figure 2.4 shows the geometrical configuration for surface diffracted rays. The surface diffracted rays become “attached”to the cylinder at the point of grazing incidence $Q_{1,3}$, at which they are tangential to the surface. Then travels through a geodesic path along the surface of distance $t_{1,2}$. As they travel over the surface the rays are attenuated exponentially

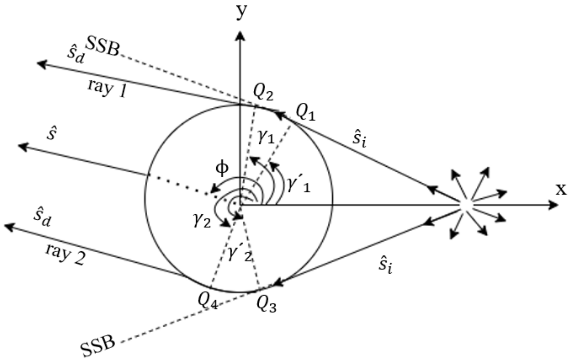

Figure 2.4: Geometrical details for the two rays surface diffraction from a circular cylinder. Image source: [23]

and also contribute to the phase change. The ray leaves the surface tangentially at shedding points $Q_{2,4}$. If the observation point,P_d is in the far zone, we refer to the observation direction ϕ rather than an observation point as such. From figure 2.4, two surface diffracted rays proceed in a given direction ϕ. The diffraction ray direction is simply the observation direction given as:

$$\hat{s}_d = cos(\phi)\hat{x} + sin(\phi)\hat{y} \tag{2.19}$$

it is same for both the ray 1 and 2.

Finding the attachment and the detachment points

The point $Q_{1,3}$ at which $\hat{n}(Q_{1,3}) \cdot \hat{s}_i(Q_{1,3}) = 0$ must hold is given by [23]:

$$\gamma_1' = \cos^{-1}(r/d) \tag{2.20}$$

r is the radius and d is the distance of the source location from the center. Symmetry leads to

$$\gamma_1 = 2\pi - \cos^{-1}(r/d) \tag{2.21}$$

The position of the shedding points for a given observation direction ϕ, are located by:

$$\hat{n}(Q_{2,4}) \cdot \hat{s}^d(Q_{2,4}) = 0 \tag{2.22}$$

which implies that

$$\gamma_2' = \phi - \pi/2 \tag{2.23}$$

$$\gamma_2 = \phi + \pi/2 \tag{2.24}$$

The length of the cylinder geodesic between Q_1((resp. Q_3)) to Q_2(resp. Q_4) is t1(resp. t2) given by:

$$t_{1,2} = \pm r[\gamma_{1,2} - \gamma'_{1,2}] \tag{2.25}$$

and the plus(or minus) sign applies if the arc length is measured counterclockwise(or clockwise)

$$t_1 = r(\gamma_1 - \gamma'_1) \tag{2.26}$$

$$t_2 = -r(\gamma_2 - \gamma'_2) \tag{2.27}$$

Incident field at the attachment points

The GO incident fields at both Q_1 and Q_3 are:

$$E^i(Q_{1,3}) = \overrightarrow{E}_{s,h} \frac{e^{-jks_i(Q_{1,3})}}{s_i(Q_{1,3})} \tag{2.28}$$

where $s_i(Q_{1,3})$ is the distance between source and the attachment point $Q_{1,3}$.

Diffracted field at the observation point

The surface diffracted field(due to ray 1 or 2) is given as [25]:

$$E^{d1,2}_{s,h}(\phi) = E^i(Q_{1,3})\overline{\overline{T}}^{1,2}_{s,h} A^{1,2}_d \sqrt{\frac{s_0}{s_0 + t_{1,2}}} e^{-jks^d} \tag{2.29}$$

where, $A^{1,2}_d$ is the spreading factor given as $1/\sqrt{s^d}$. s^d is the distance between the detachment point and the observation location. $\sqrt{\frac{s_0}{s_0 + t_{1,2}}}$ is the conservation of energy flux in the surface-ray strip from $Q_{1,3}$ to $Q_{2,4}$.

$\overline{\overline{T}}^{1,2}_{s,h}$ is the dyadic diffraction coefficient given as:

$$\overline{\overline{T}}^{1,2}_{s,h} = T^{1,2}_s \hat{e}_\perp(Q_{1,3})\hat{e}_\perp(Q_{2,4}) + T^{1,2}_h \hat{e}_\parallel(Q_{1,3})\hat{e}_\parallel(Q_{2,4}) \tag{2.30}$$

The unit vectors are calculated as follows:

$$\hat{e}_\perp(Q_{1,3}) = \frac{\hat{s}_i(Q_{1,3}) \times \hat{n}(Q_{1,3})}{\parallel \hat{s}_i(Q_{1,3}) \times \hat{n}(Q_{1,3}) \parallel} \tag{2.31}$$

$$\hat{e}_\parallel(Q_{1,3}) = \frac{\hat{e}_\perp(Q_{1,3}) \times \hat{n}(Q_{1,3})}{\parallel \hat{e}_\perp(Q_{1,3}) \times \hat{n}(Q_{1,3}) \parallel} \tag{2.32}$$

$$\hat{e}_\perp(Q_{2,4}) = \frac{\hat{s_d}(Q_{2,4}) \times \hat{n}(Q_{2,4})}{\parallel \hat{s_d}(Q_{2,4}) \times \hat{n}(Q_{2,4}) \parallel} \tag{2.33}$$

$$\hat{e}_{\parallel}(Q_{2,4}) = \frac{\hat{e}_{\perp}(Q_{2,4}) \times \hat{n}(Q_{2,4})}{\parallel \hat{e}_{\perp}(Q_{2,4}) \times \hat{n}(Q_{2,4}) \parallel} \tag{2.34}$$

$\hat{s_i}(Q_{1,3})$ is the incident vector from source to the attachment point $Q_{1,3}$. $\hat{n}(Q_{1,3})$ is the normal vector at point $Q_{1,3}$. $\hat{s_d}(Q_{2,4})$ is the vector from detachment point $Q_{2,4}$ to the observation location, $\hat{n}(Q_{2,4})$ is the normal vector at point $Q_{2,4}$.

UTD diffraction coefficients $T^{1,2}_{s,h}$ are expressed as:

$$T^{1,2}_{s,h} = -m(Q_{1,2})\sqrt{\frac{2}{k}}e^{-jkt_{1,2}}G_{s,h}(\xi_{d1,2}, X_{d1,2}) \tag{2.35}$$

The Fock parameter, $\xi_{d1,2}$ and the parameter, $X_{d1,2}$ is given as:

$$\xi_{d1,2} = \frac{m(Q_{1,3})}{r(Q_{1,3})}t_{1,2} \qquad \& \qquad X_{d1,2} = \frac{kL_d(\xi_{d1,2})^2}{2m(Q_{1,3})^2} \tag{2.36}$$

2.3.4 Interaction Coefficients

The curvature parameter m is expressed as:

$$m = \left(\frac{kr}{2}\right)^{\left(\frac{1}{3}\right)} \tag{2.37}$$

where r is the cylinder radius of curvature along the geodesic containing the point Pt. Pt is the point on the surface of the cylinder. It can be Q_r, $Q_{1,3}$, $Q_{2,4}$.

Finally, a common function $G_{s,h}(\xi, X)$ appearing in equations (2.12) and (2.30) is expressed as:

$$G_{s,h}(\xi, X) = \frac{e^{-j\pi/4}}{2\xi\sqrt{\pi}}[1 - F(X)] + \widehat{P}_{s,h}(\xi, q_{s,h}) \tag{2.38}$$

F(X) is the Fresnel integral calculated as:

$$F(X) = 2j\sqrt{X}e^{jX}\int_{\sqrt{X}}^{+\infty} e^{-jt^2}dt \tag{2.39}$$

and the Pekeris function $\widehat{P}_{s,h}(\xi)$ is given as[26][9]:

$$\widehat{P}_{s,h}(\xi, q_{s,h}) = \frac{e^{-j(\pi/4)}}{\sqrt{\pi}}\left\{-\frac{1}{2\xi} + G_1(\xi, q_{s,h}) + G_2(\xi, q_{s,h})\right\} \tag{2.40}$$

$$G_1(\xi, q_{s,h}) = \frac{e^{-j(\pi/6)}}{2}\int_0^{\infty}\frac{[e^{-j(\pi/6)}Ai'(t) + q_{s,h}e^{j(\pi/6)}Ai(t)]e^{-j\xi at}}{e^{j(\pi/6)}Ai'(te^{j(2\pi/3)}) + q_{s,h}e^{-j(\pi/6)}Ai(te^{j(2\pi/3)})}dt \tag{2.41}$$

$$G_2(\xi, q_{s,h}) = -\frac{1}{2}\int_0^\infty \frac{[Ai'(t) - q_{s,h}Ai(t)]e^{-j\xi t}}{e^{j(\pi/6)}Ai'(te^{-j(2\pi/3)}) + q_{s,h}e^{-j(\pi/6)}Ai(te^{-j(2\pi/3)})}dt \tag{2.42}$$

wherein, $a = e^{-j2\pi/3}$

$$q_s = -jm(Pt)K \tag{2.43}$$

$$q_h = -j\frac{m(Pt)}{K} \tag{2.44}$$

$$K = \sqrt{\epsilon_r} = \sqrt{\epsilon_r' - j\left[\epsilon_r'' + \frac{\sigma}{2\pi f_c 8.85e^{-12}}\right]} \tag{2.45}$$

ϵ_r' and ϵ_r'' are the real and imaginary relative permittivity values. σ is the conductivity. f_c is the operating frequency. Pekeris function is the only function that takes into consideration of the dielectric property of the human body.

2.3.5 Total Electric Field

Finally, the total received electric field is computed using the following expression:

$$E^T_{s,h}(\phi) \simeq \alpha E^i_{s,h}(\phi) + \beta_r E^r_{s,h}(\phi) + \sum_{n=1}^{2}\beta_d E^{dn}_{s,h}(\phi) \tag{2.46}$$

$$\alpha = \begin{cases} 1, & \text{lit region} \\ 0, & \text{shadow region} \end{cases}$$

$$\beta_r = \begin{cases} 1, & \text{lit region} \\ 0, & \text{shadow region} \end{cases}$$

$$\beta_d = \begin{cases} 1, & \text{shadow region} \\ 0, & \text{lit region} \end{cases}$$

n in equation 2.46 is the number of rays. In this project two-ray diffraction model is used therefore n=2.

2.3.6 Total Received Power Calculation

Total received electric field is the vector sum of the soft and hard received electric components:

$$E_{total} = \sqrt{|E^T_s|^2 + |E^T_h|^2} \tag{2.47}$$

According to the Frii's free space equation the received power is calculated as:

$$P_r[dBm] = P_t[dBm] - FSL[dB] + G_t[dB] + G_r[dB] + Lprop[dB] \tag{2.48}$$

where, P_t is the transmit power, G_t is the transmitting antenna gain, G_r is the receive antenna gain, FSL is the Free Space Loss given as:

$$FSL = 20log_{10}\left(\frac{4\pi r f_c}{c}\right) \tag{2.49}$$

f_c is the operating frequency. r is the distance in meters. c is the velocity of light in free space. L_{prop} is given as:

$$L_{prop} = 20log_{10}(E_{total}) \tag{2.50}$$

2.4 Applying UTD Model to Human body

While modelling the human body we should consider two important aspects. Firstly, the geometrical approximation and secondly the electromagnetic properties of the human body. The height-dependent human body geometrical approximation is as shown in Figure 2.5. In the figure, h_{head}, h_{torso}, h_{leg} is the height of the cylinder at head, torso, and leg level. The height of each cylinder is assumed according to the structure of the human body. The radius at head, torso, aand leg is denoted as r_{head}, r_{torso}, r_{leg} respectively which is assumed based on the radius of the minimum enclosing sphere of the human body at respective heights.

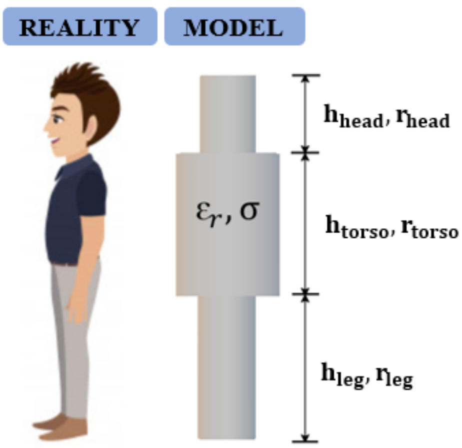

Figure 2.5: Human body modelled as a three joint circular cylinders of different radius

The relative permittivity and conductivity are selected based on the skin model measurement from the literature [18] wherein permittivity and conductivity of the human skin are measured using swept-frequency network and impedance analyzers in the frequency range 10Hz to 20GHz. The skin model is chosen as the scattering is observed at the human body skin level. As seen in Figure 2.6 both permittivity and conductivity is frequency-dependent. When the frequency increases the conductivity of the human skin increases and the permittivity decreases.

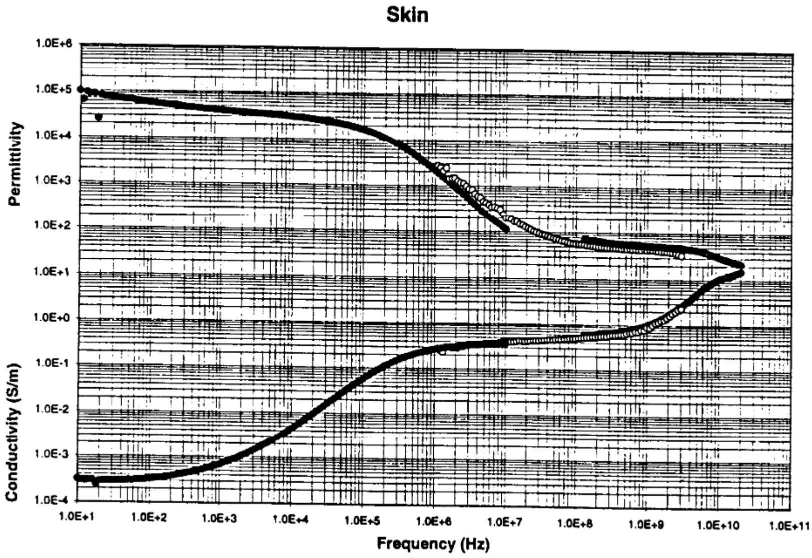

Figure 2.6: Permittivity and conductivity values of the human skin at different frequencies. Image source: [18]

The UTD solution for the dielectric circular cylinder is applied separately for each cylinder during the simulation. All three cylinders are assumed to have homogeneous dielectric properties. The input parameters of the simulation model are frequency, the radius of the cylinder at different heights, the distance between the source, and the center of the cylinder, permittivity and conductivity.

3 Measurement Campaign

In this section details of the measurement scenario, system specifications, system calibration, and data processing procedure of the measured data are discussed.

3.1 Measurement Setup

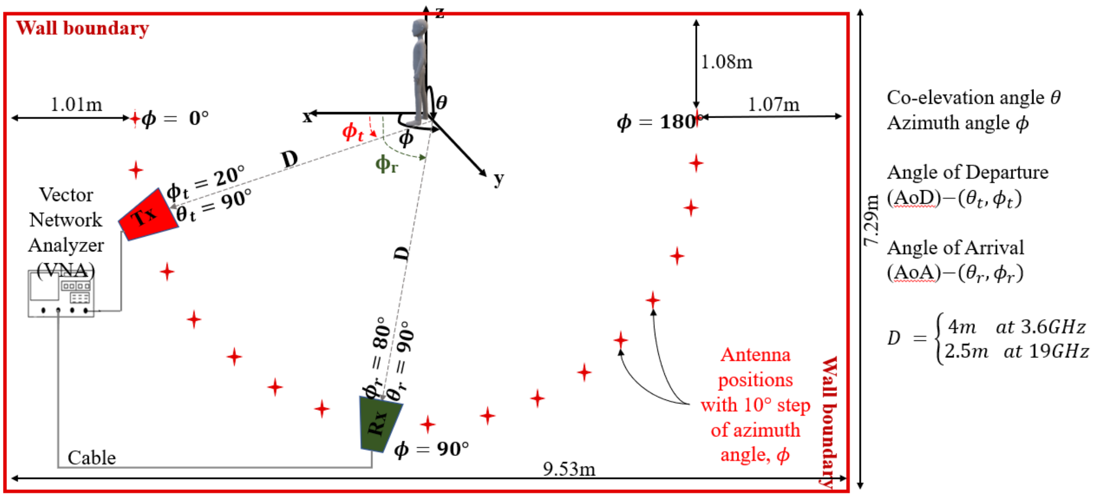

Figure 3.1: Two dimensional floor plan of the measurement setup

The measurement campaign was conducted in a large empty room on the 4th floor of carré building inside the University of Twente campus as illustrated in Figure 3.1. The human body is stationary and is at the center of observation semi-circle throughout the experiment. The measurement was planned in detail to avoid the reflections from walls and other objects that interfere with the signal from the human body. The distance between the human body/antennas and the sidewalls of the room is at least 1m. Furthermore, there is no scatterer in the proximity of the human body or antennas. Directional horn antennas are used to avoid the interference from the multipath signals. The transmitting and receiving antennas are at equal distance from the human body and always directed towards the human body. The point and cross lasers are used to improve the accuracy of the antenna's orientation and positioning towards the human body. These lasers are mounted on the center of both the transmitting and receiving antennas which can be seen in Figure 3.2. In the same setup, the measurement was also done on a cylindrical object of height 34cm and diameter 23.5cm. The metallic cylinder object is placed approximately 1.4m above the ground level on a platform to avoid reflections from the ground.

(ϕ_t, θ_t) is the Angle of Departure(AoD) at the transmitting antenna and (ϕ_r, θ_r) is the Angle of Arrival(AoA) at the receiving antenna. The azimuth angles of both the transmitting and receiving antenna are varied from 0° to 180° at a step of 10°. The co-elevation angle of both the transmitting and receiving antenna is fixed at 90°. Both position and orientation of the human body are unchanged throughout the measurement campaign. The orientation of the human body is based on the antenna reciprocity assumption.

(a) Torso level measurement at 3.6GHz

(b) Head level measurement at 3.6GHz

(c) Cylinder measurement at 19GHz

Figure 3.2: Channel measurement with the presence of the human body & Cylinder

3.2 System Specifications

The system parameters and its values are described in Table 3.1. The human body measurement was done at two frequencies, 3.6GHz and 19GHz and the cylinder measurement was done only at 19GHz. The 2GHz bandwidth is chosen to have a high delay resolution. Both the transmitting and receiving antennas are located on an observation semi-circle with a human at the center. The radius of the observation semi-circle satisfies the Fraunhofer far-field criteria:

$$D > \frac{2d^2}{\lambda}$$

d is the largest dimension of the antenna, λ is the wavelength. The largest dimension of the Dual ridge horn antenna is 34.45cm and the Rectangular horn antenna is 7.77cm. The human body measurement is done at three heights - head, torso and leg level of the human body. The heights chosen are specific to the physical measurement of the subject.

System specification

	Human body	Cylinder
Antenna height 1 [m]	1.59	1.56
Antenna height 2 [m]	1.10	NA
Antenna height 3 [m]	0.81	NA
Center frequency 1 [GHz]	3.6	NA
Center frequency 2 [GHz]	19	
Bandwidth [GHz]	2	
Frequency points	801	
Time resolution [ns]	0.5	
Power [dBm]	0	

Table 3.1: Details of the system parameters

Figure 3.3 depicts the two UWB directional horn antennas used during the measurement and its specifications are mentioned in Table 3.2. More details on the antennas can be referred from the website [27][28]. The transmit power is within the Maximum Permissible Exposure(MPE) limits of the human body in the controlled environments specified by "IEEE Standard for Safety Levels with Respect to Human Exposure to Radio Frequency Electromagnetic Fields, 3 kHz to 300 GHz"[29] and also in the detectable range of the receiving antenna.

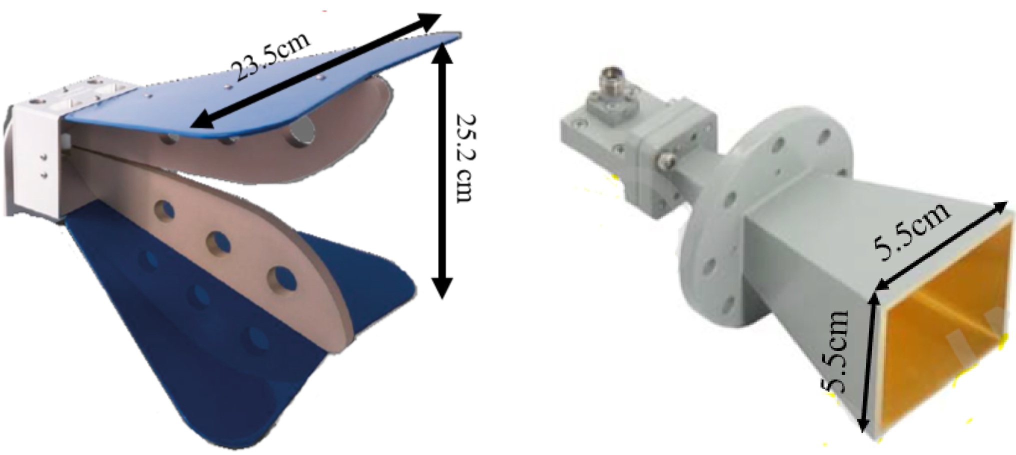

(a) Dual ridge horn antenna (b) Rectangular horn antenna

Figure 3.3: Ultra Wide Band(UWB) directional horn antennas.

3.3 System Calibration

The transmitting and receiving antennas are connected to the Agilent VNA which operates up to 20GHz. Before starting the measurement, the traditional two-port SOLT(Short

Antenna specification

Parameters	**Dual ridge horn**	**Rectangular horn**
Frequency range [GHz]	0.7 - 18.0	18.0 - 40.0
Gain [dBi]	10.0	17.5
3 dB beamwidth [deg]	Vertical: 16.0 Horizontal: 20.0	Vertical: 20.5 Horizontal: 24.02
Dimension [L x W] [cm]	[23.5 x 25.2]	[5.5 x 5.5]

Table 3.2: Technical details of the antenna

Open Load Through) calibration was done using the calibration kit. The calibration kit comprises three impedances- Short, Open, Load, and one Transmission standards to define the calibrated reference plane. After calibration, the Line of Sight measurement was done at 3.6GHz and 19GHz. The theoretical received power is calculated using Frii's transmission equation:

$$P_{RX}|_{dBm} = P_{TX}|_{dBm} + G_{RX}|_{dB} + G_{TX}|_{dB} - FSP|_{dB} \tag{3.1}$$

FSP is the free space loss factor given as:

$$FSP|_{dB} = 20log_{10}\Big(\frac{\lambda}{4\pi R}\Big) \tag{3.2}$$

λ is the wavelength, R is the distance between transmitting and receiving antennas. Theoretically, P_{RX} = -41.62dBm at 3.6GHz, R = 7.5m and $P_{RX} = -36.99$dBm at 19GHz, R = 3.6m for the antenna gain and transmit power given in the Table 3.2 and 3.1. The SNR is measured by taking the ratio of highest received power and the average noise floor. For the measurement data shown in Figure 3.6 the SNR estimated is 46dB and for Figure 3.7 is 38.24dB.

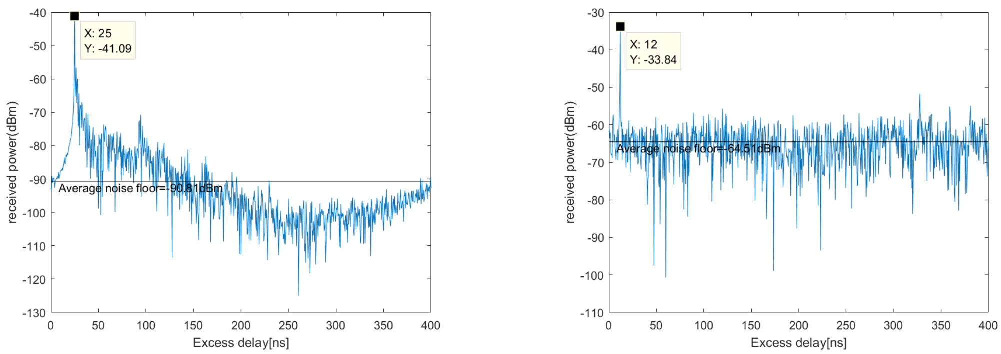

(a) f = 3.6GHz, R = 7.5m, SNR = 30.67dB (b) f = 19GHz, R = 3.6m, SNR = 49.72dB

Figure 3.4: Power Delay Profile of LoS measurement conducted after system calibration

3.4 Data Processing

Figure 3.5 shows the flowchart of the measurement data processing. The VNA measures the S-parameters of the channel for the given frequency band. The measured S21 parameter is the channel gain in the frequency domain. The S21 is converted to the time domain by applying the Inverse Fast Fourier Transform(IFFT) in MATLAB. The obtained Power Delay Profile(PDP) is time-gated to extract the delay bins relevant to the human body. The time gating delay range is the range between the minimum and maximum delay of a signal from the human body. The radius of the minimum enclosing sphere of the human body at a head, torso, and leg level is taken as the radius of the approximated cylinder. It is considered to be 0.1m, 0.2m, and 0.15m at head, torso, and leg level. This approximation of the human body radius is used only to extract delay bins relevant to human body from the channel measurement. The distance between the antennas and the human body, approximated radius are the variables used to calculate the minimum and maximum delay. The time gating delay range for the different heights and frequency is given in Table 3.3. The Figure 3.6(c) & 3.7(c) illustrates the time gating. In Figure 3.6(c) the highest peak falls outside the time gating delay range of the head and hence it is not part of the time gating. This peak could be from the torso as antenna beamwidth does not cover just the head.

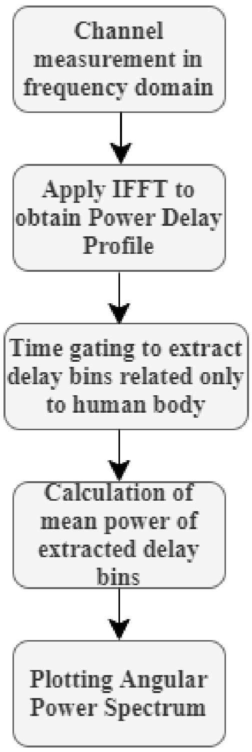

Figure 3.5: Flowchart for the data processing of the measurement data

Time gating delay range [ns]		
	3.6GHz	**19GHz**
Head	26.0 - 27.5	16.0 - 17.0
Torso	25.5 - 28.0	15.5 - 17.5
Leg	25.5 - 27.5	15.5 - 17.5

Table 3.3: Time gating delay range for different heights of the human body.

Mean power of time gated delay bins is estimated using the formula below:

$$\bar{P} = \frac{\sum_{i=1}^{N} P_i * \tau_i}{\sum_{i=1}^{N} \tau_i}$$

The mean power is calculated for each AoA and AoD resulting in Angular Power Spectrum as shown in figure 3.6(d) & 3.7(d).

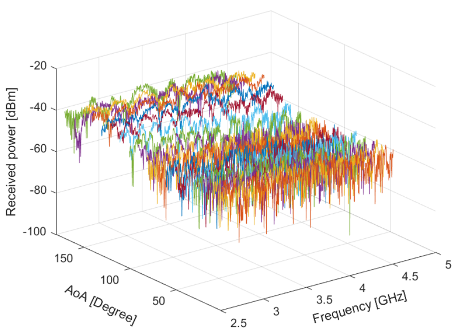

(a) S21 in frequency domain

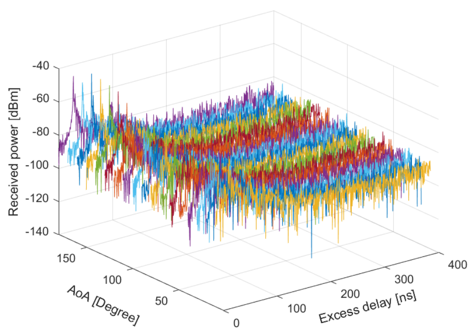

(b) Power Delay Profile

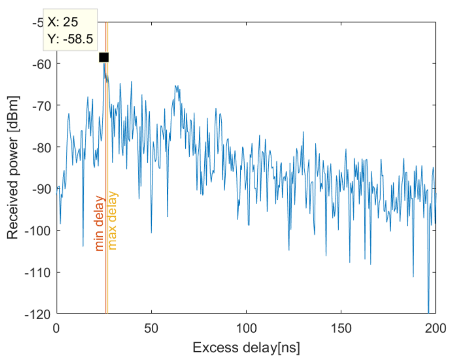

(c) Time gating applied for AoA 20°

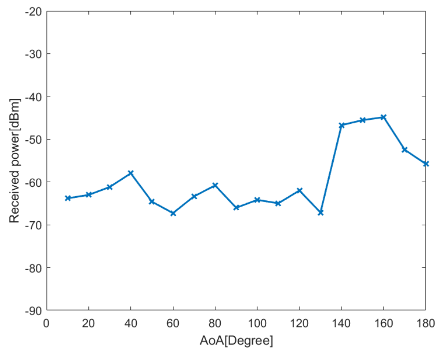

(d) Angular Power Spectrum

Figure 3.6: Illustration of head level measurement data processing at 3.6GHz for AoD 0°

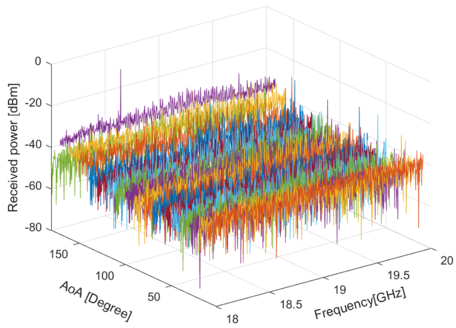

(a) S21 in frequency domain

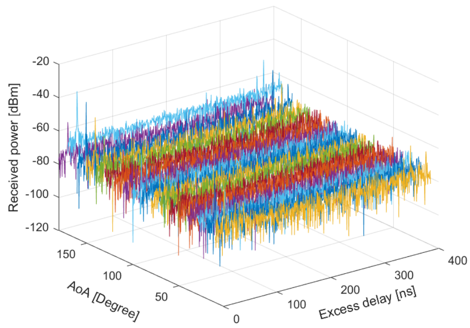

(b) Power Delay Profile

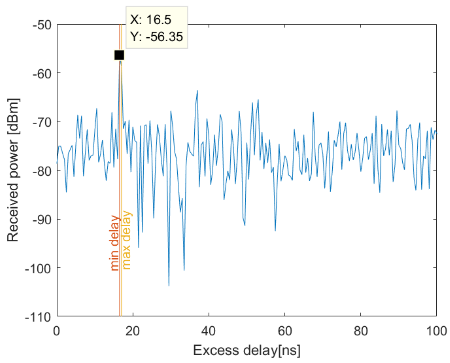

(c) Time gating applied for AoA 40°

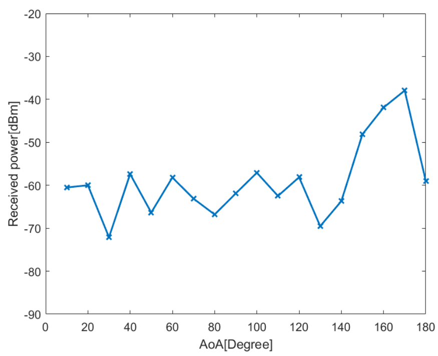

(d) Angular Power Spectrum

Figure 3.7: Illustration of head level measurement data processing at 19GHz for AoD 0°

4 Numerical Examples

This section discusses the measurement and simulation results. It includes measurement data analysis, simulation model verification, comparison between simulation and measurement results, results of parameterization.

4.1 Measurement Results and Analysis

The purpose of this experiment was to measure the human body scattering at observation semi-circle around the human body at three different heights. Both the transmitting and receiving antennas are at the same height and the antenna's aperture is oriented towards the human body center from the same distance. The missing data points in the plots at certain angles is because both the transmitting and receiving antennas could not be placed at the same location.

4.1.1 Angular Power Spectrum

The angular power spectrum estimated from the measured channel gain at each AoD and AoA is as shown in Figure 4.1 and 4.2 for 3.6GHz and 19GHz respectively. The received power is measured at 18 AoA(excludes the angle at which the transmitting antenna is located). There is gradual power level increase approx up to 20dB at AoA $0° - 40°$ and $160° - 180°$ while AoD is between $160° - 180°$ and $0° - 40°$ respectively. This is due to the occurrence of obstructed LoS scenario. The later means that both transmitting and receiving antennas are facing each other establishing a Line of Sight(LoS) link which is partially shadowed by the human body as the beamwidth of antennas are larger than the width of the human body. The scattered field is dominant at AoA 40° - 160° and LoS signal is dominant after AoA: 160° and before AoA:40°. Similar observations are made at both 3.6GHz and 19GHz. From both the figure it can be observed that the power level at certain AoA varies for different AoD.

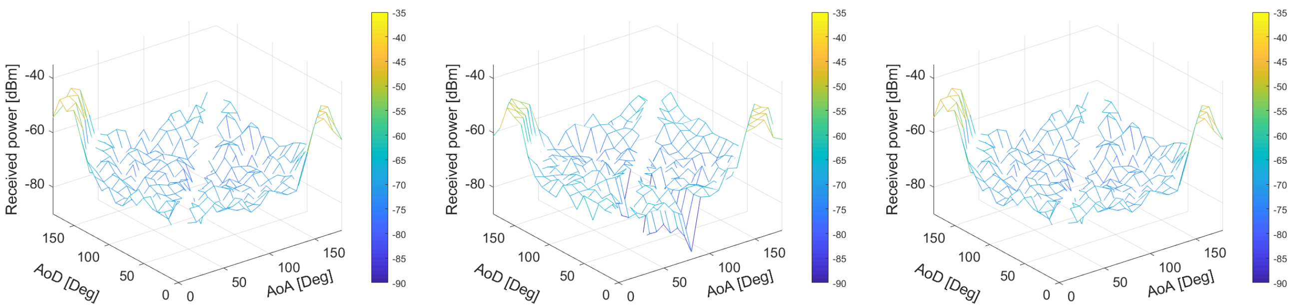

(a) Head level (b) Torso level (c) Leg level

Figure 4.1: Angular power spectrum at 3.6 GHz

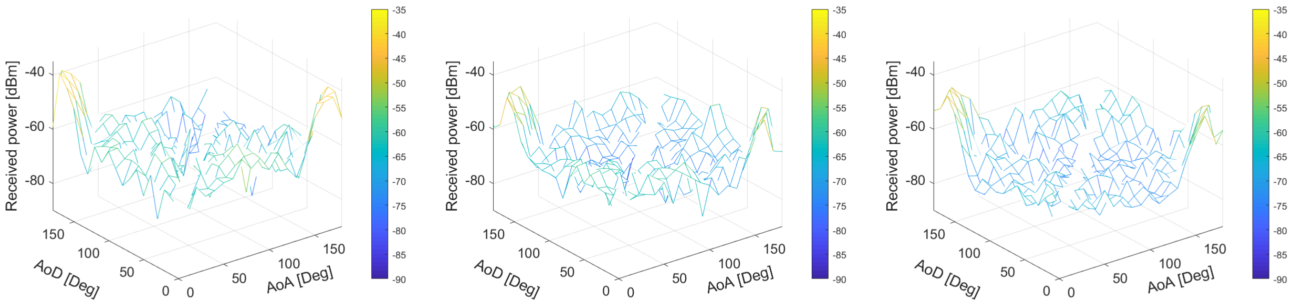

(a) Head level (b) Torso level (c) Leg level

Figure 4.2: Angular power spectrum at 19 GHz

4.1.2 Measured Human Body Attenuation at Head, Torso and Leg Level

Human body attenuation is calculated from the measured APS. Friis transmission equation for the received power is written as:

$$P_{RX}|_{dBm} = P_{TX}|_{dBm} + G_{RX}|_{dB} + G_{TX}|_{dB} - FSP|_{dB} - SL_{human}|_{dB} \tag{4.1}$$

The additional term, SL_{human} is the scattering loss caused by the human body. To obtain the scattering loss, the antenna gain, transmit power and free space loss factor are eliminated from the received power. Equation 4.1 is re-arranged to get the equation for scattering loss as:

$$SL_{human}|_{dB} = P_{TX}|_{dBm} + G_{RX}|_{dB} + G_{TX}|_{dB} - FSP|_{dB} - P_{RX}|_{dBm} \tag{4.2}$$

The obtained scattering loss in decibels is converted to a linear scale as given below for further data manipulation:

$$SL_{human}|_{linear} = 10^{SL_{human}|_{dB}/10} \tag{4.3}$$

The above equations are used to calculate the human body attenuation from the APS. The APS is a matrix of dimension $[APS]_{19X18}$, where 19 is the number of AoD and 18 is the number of AoA. The range of human attenuation at each AoA, human attenuation averaged over all the AoD at all the three heights compared to the Free Space Loss(FSL) is seen in Figure 4.3. It is observed that there is a gradual decrease in average attenuation approx. 10dB to 15dB around AoA:$0° - 40°$ and $140° - 180°$. This could be due to the influence of the obstructed LoS scenario explained earlier. Since the distance travelled by LoS signal and the human scattered signal is nearly the same wherein the LoS signal is more dominating, it is possible that the human scattering loss is influenced by LoS signal at these angles at both 3.6GHz and 19GHz. The FSL is calculated using equation 3.2. At 3.9GHz, the FSL is 61.62dB for a distance of 8m and at 19GHz, the FSL is 72dB for a distance of 5m. The FSL is nearly 30dB higher than the human attenuation at both 3.6GHz and 19GHz meaning that at given distance and frequency FSL is more dominating.

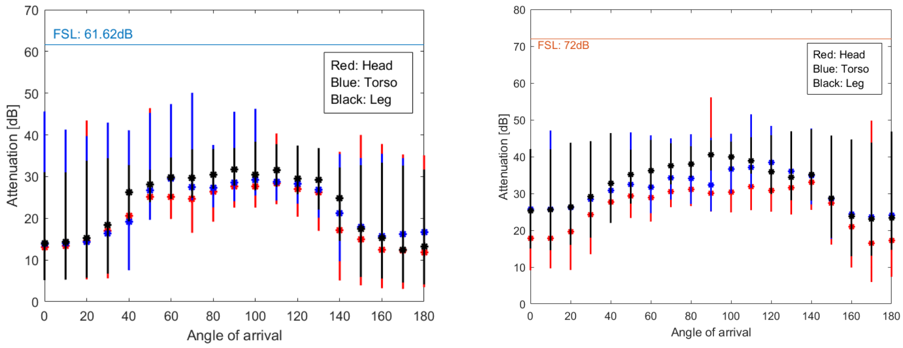

(a) 3.6GHz (b) 19GHz

Figure 4.3: Comparison of FSL and human attenuation averaged over AoD at 3.6GHz and 19GHz

It is also observed that the attenuation at the leg level is higher than the head and torso level by 1dB - 2dB. There can be two reasons for the lowest received power level at leg height: 1. Electromagnetic wave interaction with a different forms of human body composition ex: higher bone density and less fat and 2. Could be due to the destructive interference caused by the signals received from the two legs. The Fresnel zone computation has proved that there is no possibility of ground reflection. The Fresnel zone radius is calculated using the formula:

$$F[m] = 6.656\sqrt{\frac{D[km]}{f[GHz]}}$$

F is 12.9μm at 3.6GHz for a distance of 8m and 5μm at 19GHz for a distance of 5m.

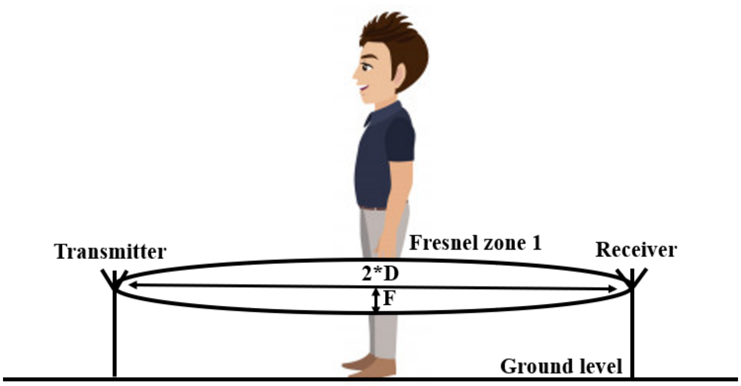

Figure 4.4: Fresnel zone calculation at leg level

4.1.3 Comparison of Human Body Attenuation at 3.6GHz and 19GHz

The empirical cumulative distribution function is plotted for the human body attenuation averaged over all AoD as seen from Figure 4.5. It is observed that the human attenuation is approximately 10dB higher at 19GHz at all three heights. The attenuation averaged over all AoA and AoD is also computed for all the heights and tabulated in the Table 4.1. From Table 4.1, attenuation at head level is observed to be the lowest compared to the torso and leg level at both 3.6GHz and 19GHz.

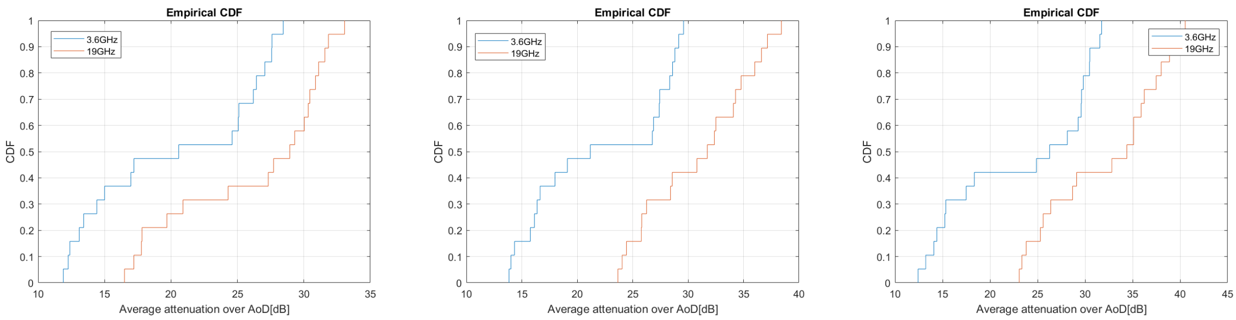

(a) Head level (b) Torso level (c) Leg level

Figure 4.5: Empirical Cumulative Distribution Function of attenuation averaged over AoD at 3.6GHz and 19GHz

Average attenuation [dB]		
Height	**3.6GHz**	**19GHz**
Head	16.88	22.62
Torso	18.84	28.73
Leg	18.47	28.71

Table 4.1: Average attenuation over all Angles of Departure and Angles of Arrival

4.2 Simulation Results

The simulation model is first verified using the existing examples from the literature and then used for the human body modelling. Therefore this section contains the results from the model verification, followed by simulation model comparison with measurement.

4.2.1 Verification of UTD Model

The simulation results of a UTD circular dielectric cylinder model was compared with a textbook [23] and a literature [9] examples. All the UTD equations from section 2.3 are used except a few equations such as 2.4,2.47-2.50 which are specific to the measurement scenario of this project.

Figure 4.6-4.8 are the simulation results for an example from the textbook. In this example, the electric field pattern of the conducting circular cylinder illuminated by a TE and TM polarized electric field is computed for the lit region and shadow region. The radius of the cylinder is λ, the distance between the observation point and the cylinder center is 2λ. The operating frequency is 1MHz. Since the conducting cylinder is assumed, the values of the relative permittivity, $\epsilon_r = 1$, and conductivity $\sigma = 10^7$ are assigned based on the material properties given for metal from the ITU-R literature [29]. For the lit zone, the reflection coefficient of GO and UTD both are verified.

Figure 4.9-4.10 are results for the specification given in the literature [9]. In this example, the simulation is done for a dielectric circular cylinder model with $\epsilon_r = 48.2$ and $\sigma = 4.7$ at center frequency 4.5GHz. The cylinder radius is 3.5cm and the distance from the cylinder and the source point is 7cm. The latter values are according to the measurement performed in the literature. The antenna pattern information used in the literature are not provided and hence not used in our simulation. Therefore the results are not exactly the same as in the literature.

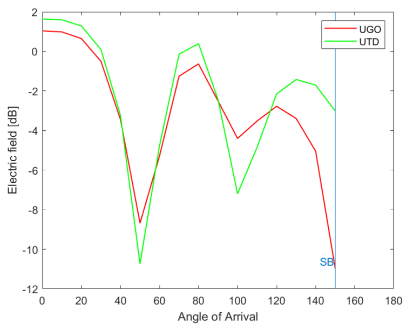

(a) Simulation results

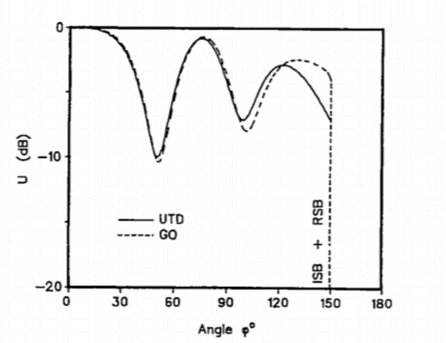

(b) Textbook example

Figure 4.6: Electric field pattern of the conducting circular cylinder illuminated by a TM polarized electric field in lit zone.

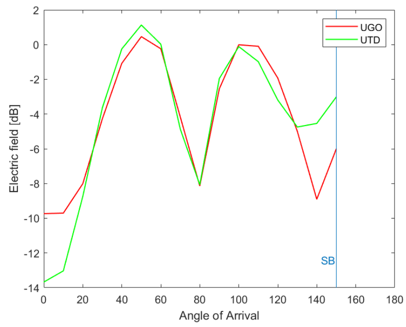

(a) Simulation results

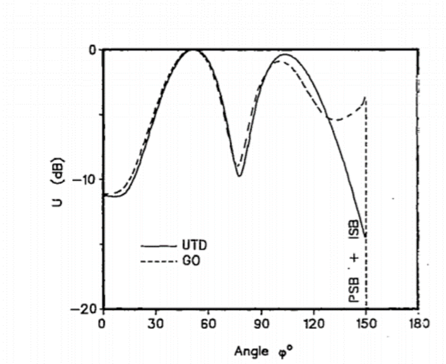

(b) Textbook example

Figure 4.7: Electric field pattern of the conducting circular cylinder illuminated by a TE polarized electric field in lit zone.

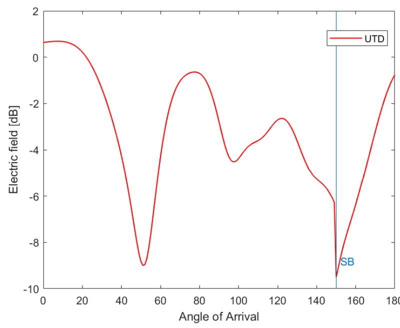

(a) Simulation results

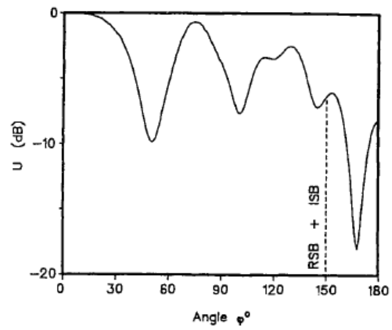

(b) Textbook example

Figure 4.8: Electric field pattern of the conducting circular cylinder illuminated by a TM polarized electric field with surface-diffracted ray contributions included in the lit zone.

(a) Simulation results

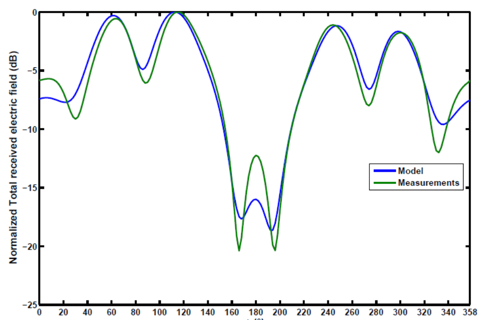

(b) literature example

Figure 4.9: Verification of simulation model

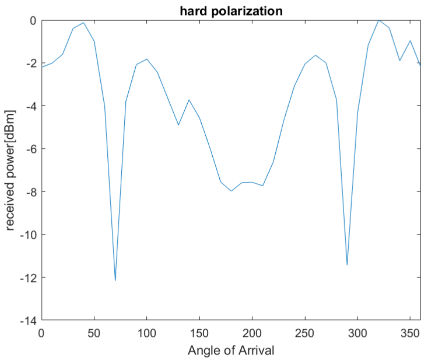

(a) Simulation results

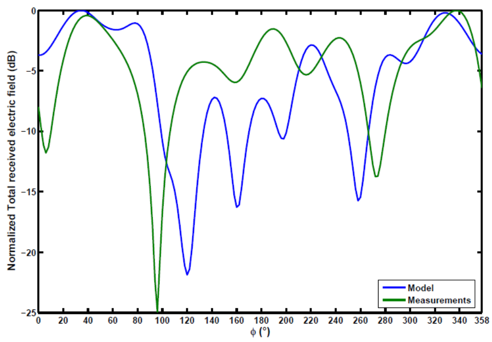

(b) literature example

Figure 4.10: Verification of simulation model

4.2.2 Three Electric Field Components of the Total Electric Field

The total electric field mainly comprises three distinct electric field components: direct field, reflected field, and the diffracted field as shown in Figure 2.2. The intensity of these fields varies based on the location of the observation point. In the lit region, the direct and reflected field is more dominant than the surface diffracted field. Whereas in the shadow region, the diffracted field is dominant and there is an absence of direct and reflected field. This theory is verified through the simulation model specifically for the measurement scenario of this project. All the equations used in the simulation are discussed in section 2.3. During the measurement campaign, two-directional antennas were used for both transmitting and receiving. The approximated directivity of these antennas is provided using equation 2.4. This is because the radiation pattern of the antennas used was not available. Figure 4.11 illustrates the three electric field component pattern observed from an observation semi-circle with a cylinder located at the center of the observation semi-circle as shown in Figure 3.1.

The simulation results for AoD: 0° is seen in 4.11(a). Due to the directional property of the antenna, direct field increases at angles starting from approximately 160°. This is because the antennas are aligned at these angles establishing a LoS link. The surface diffracted field is negligible compared to the reflected field in the lit region which is in accordance with the theory. In 4.11 (b), results for AoD: 90° is seen. In this scenario, antenna directivity transmitting and receiving antennas don't align with each other at any angles to establish LoS link. Therefore reflected field component is more dominant than the direct field. The diffracted field is negligible and increases gradually on either side of the AoA: 90° as the antenna move toward the shadow region. The electric field intensity of these three components affects the total electric field at each AoA.

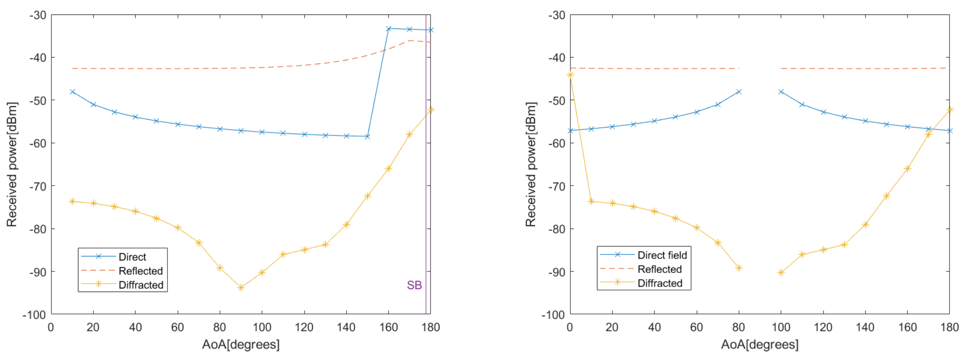

(a) AoD: 0°　　(b) AoD: 90°

Figure 4.11: Direct, Reflected and diffracted components of the total electric field at f_c: 19GHz, r = 0.1m, d= 4m

4.3 Comparison Between Measurement and Simulation Results

Figure 4.12 illustrates the measurement-based modelling and parameterization technique. The estimation of APS from the channel measurement is explained in section 3. On the other hand, simulated APS is calculated for the dielectric circular cylinder by applying the UTD solution for the given frequency, associated dielectric values, and radius. The power normalisation is done for simulated APS using equation 2.48. The assumed complex dielectric values for the simulation is given in the table 4.2:

Complex dielectric parameters

Frequency	ϵ_r	σ
3.6GHz	65	4
19GHz	40	15

Table 4.2: Permittivity and conductivity assumed at 3.6GHz and 19GHz

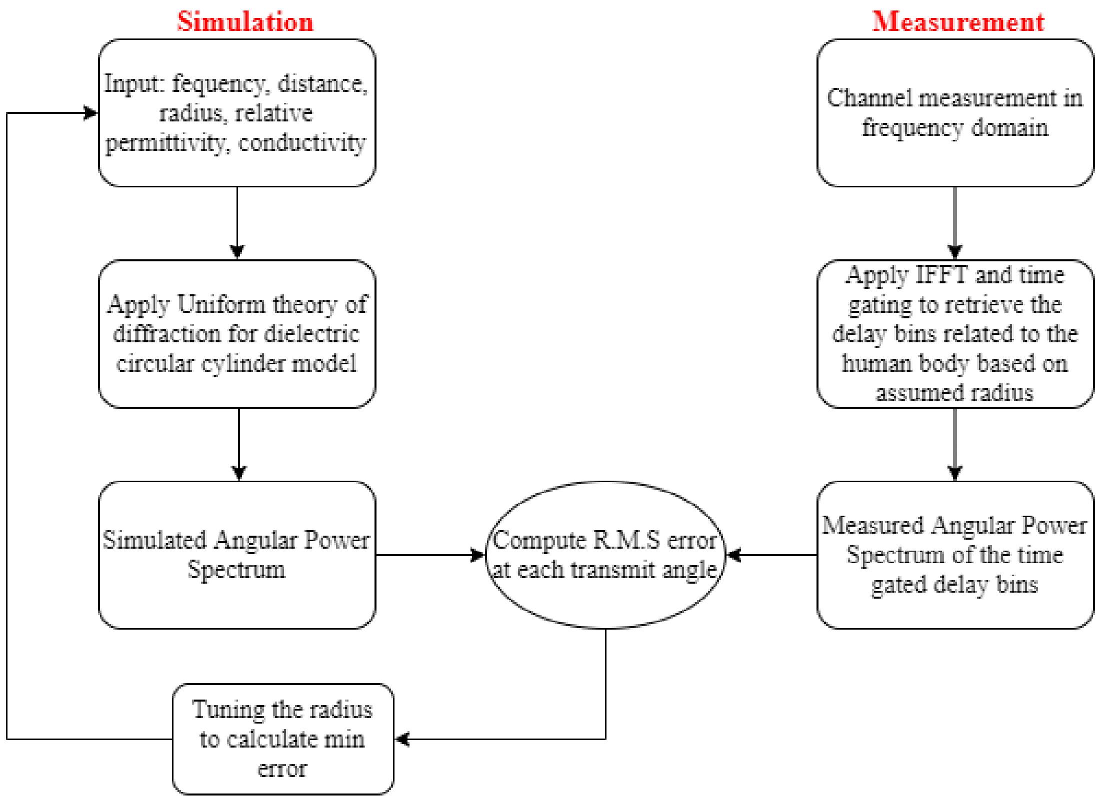

Figure 4.12: Measurement based modelling & parameterization methodology

Both the measured and simulated APS at each AoD is normalized by the maximum value of the APS before calculating the RMSE. The RMSE between the measured APS and the simulated APS is estimated to evaluate the accuracy of the simulation model for every AoD. The equation for the RMSE is given below:

$$RMSE = \sqrt{\frac{\sum_{t=1}^{T}(P_{meas} - P_{sim})^2}{T}} \tag{4.4}$$

where, T is the number of receiver positions. The radius of the simulation model is tuned to find the least RMSE between simulated and measured APS.

4.3.1 Simulation Results Compared with Cylinder Measurement Results

To observe the scattering pattern of the cylindrical object for different AoD, cylinder measurement was performed at three AoD: 0°, 90° and 180°. The delay bins relevant to the cylinder are extracted from the delay range $16ns$ to $17ns$ using time gating. This measurement was done at 19GHz for two reasons: (a) the directivity of rectangular horn antenna is better than ridge horn antenna and (b) the dimension of the cylinder becomes electrically large at this frequency. Figure 4.13 illustrates the comparison between measurement and simulation results. The pattern of the simulation results closely matches the measurement results. The RMSE is calculated as explained in the previous section and tabulated in Table 4.3. The lowest RMSE proves that the simulation model is fitting well with the measurement results.

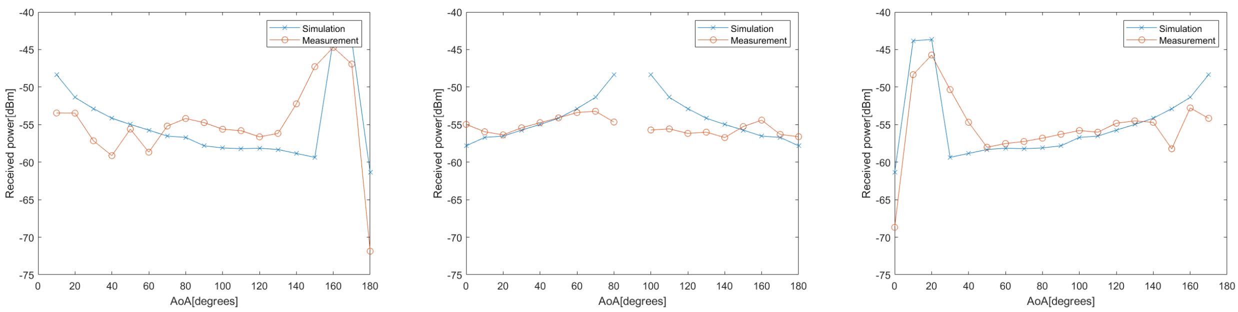

(a) AoD: 0° (b) AoD: 90° (c) AoD: 180°

Figure 4.13: Comparison between measurement and simulation results of a conducting cylinder at 19GHz, r =0.1m, D = 2.5m

RMSE

AoD	**Error**
0°	0.16
90°	0.40
180°	0.13

Table 4.3: RMSE calculated between measured and simulated APS of cylinder at three AoD

4.3.2 Simulation Results Compared with Human body Measurement Results

In this section, a few examples are presented to illustrate the comparison between simulated APS and measured APS at head, torso, and leg level for different AoD. Figure 4.14 and 4.15 depicts the comparison at 19GHz for head and torso level. Figure 4.16 is for leg level comparison at 3.6GHz. From the given examples, by visual inspection, it is observed that for any AoD between $40° - 160°$ the measurement results deviate largely. At these angles, the antennas are directed towards the side plane of the human body. The simulation and measurement results are closely matching at angles such as $0°, 20°, 180°$, etc. At these angles, antennas are oriented towards either front or back plane of the human body. This proves that the cylinder approximation of the human body is valid at only certain AoD.

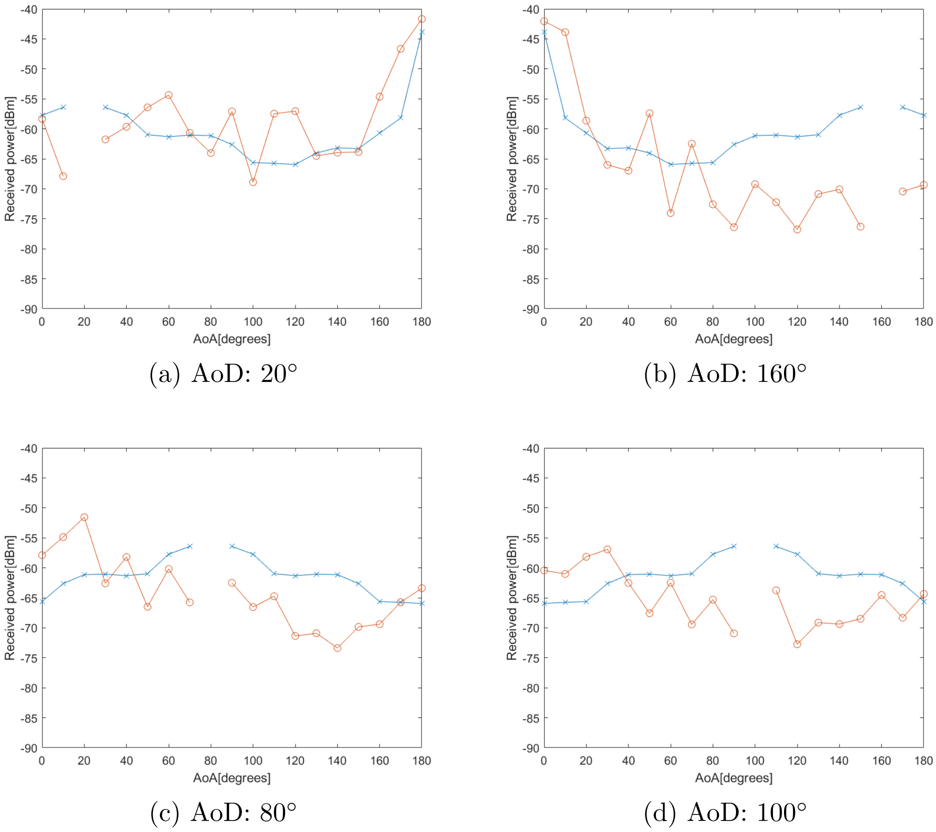

(a) AoD: 20°

(b) AoD: 160°

(c) AoD: 80°

(d) AoD: 100°

Figure 4.14: Comparison between measurement and simulation results at 19GHz for head level. r=0.1m,D=2.5m

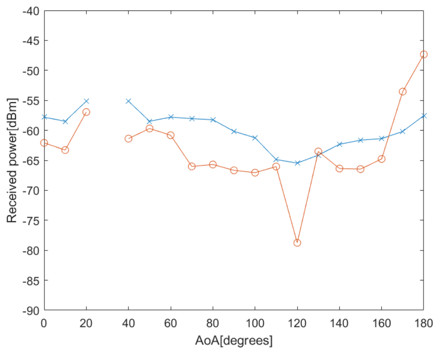

(a) AoD: 30°

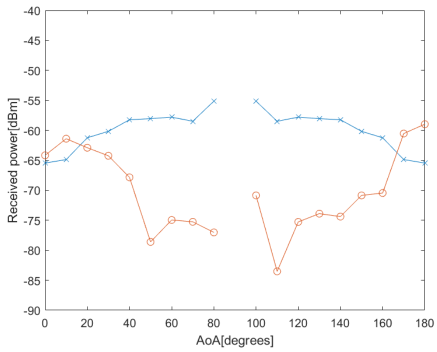

(b) AoD: 90°

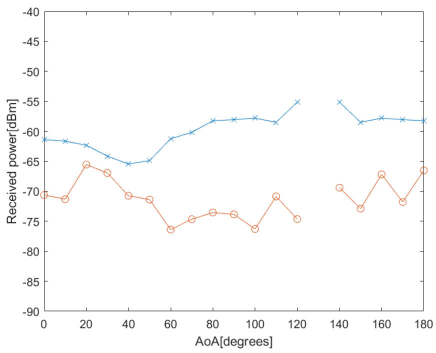

(c) AoD: 70°

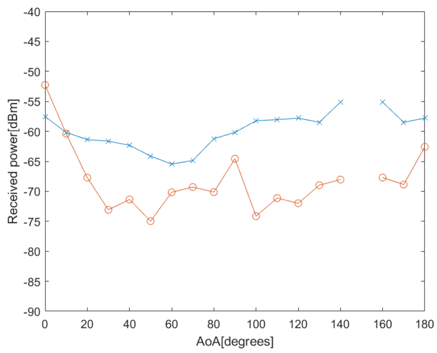

(d) AoD: 110°

Figure 4.15: Comparison between measurement and simulation results at 19GHz for torso level. r=0.2m, D=2.5m

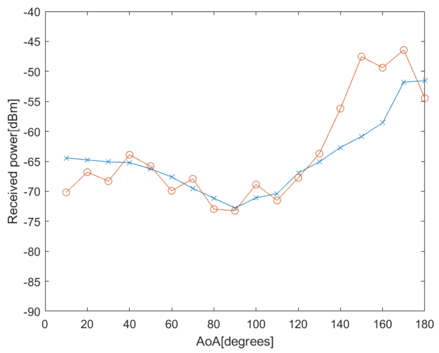

(a) AoD: 0°

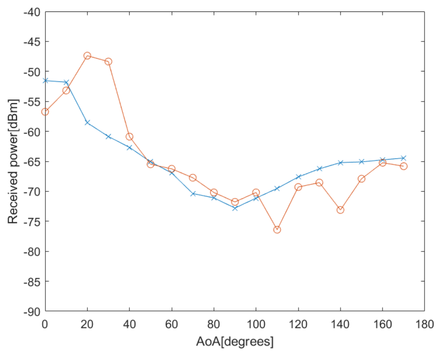

(b) AoD: 180°

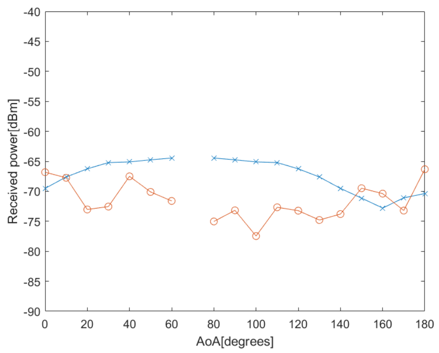

(c) AoD: 70°

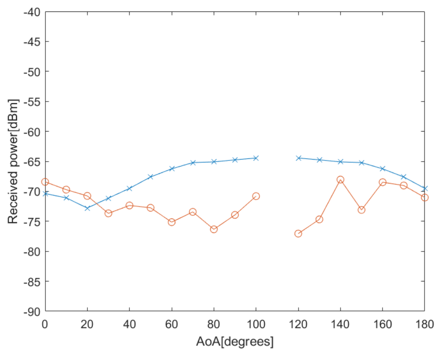

(d) AoD: 110°

Figure 4.16: Comparison between measurement and simulation results at 3.6GHz for leg level. r=0.15m, D=4m

4.4 Parameterization

To compute the radius that best fits at all the angles around the human body observed from the observation semi-circle, RMSE is computed between the measured and simulated APS at each AoD for different radius. Figure 4.17 and 4.18 depicts the RMS error at AoD $0° - 180°$. The RMSE plot indicates the accountability of the cylinder simplification at different AoD. It is observed that the error is high between $40° - 160°$ at all three heights.

The RMSE is averaged[30] over all AoD to find the radius that is suitable from all the angles around the human body. The standard deviation [31] is calculated to find the deviation of the radius over this mean value. It is observed that the best fit radius at head, torso, and leg level is different for 3.6GHz and 19GHz. At 3.6GHz, the best fit radius is 0.06m, 0.30m and 0.10m at the head, Torso and leg level respectively. At 19GHz, the best fit radius is 0.11m, 0.15m, and 0.15m at head, Torso and leg level respectively. The best fit radius for the leg is the same as the torso level at 19GHz.

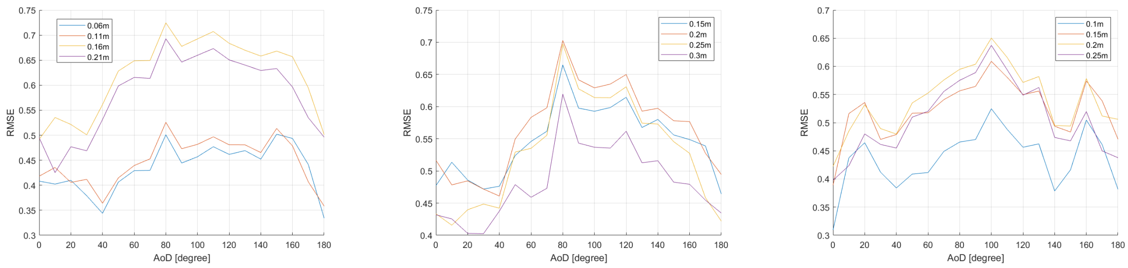

(a) Head (b) Torso (c) Leg

Figure 4.17: Radius parameterization at different transmitter angles at frequency 3.6GHz

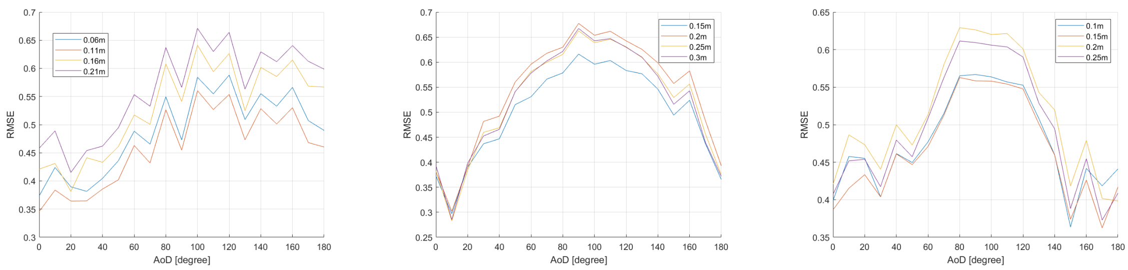

(a) Head (b) Torso (c) Leg

Figure 4.18: Radius parameterization at different transmitter angles at frequency 19GHz

Head level				
Radius [m]	***3.6GHz***		***19GHz***	
	Mean RMSE	***Standard Deviation***	***Mean RMSE***	***Standard Deviation***
0.06	0.43	0.04	0.48	0.07
0.11	0.44	0.04	0.45	0.06
0.16	0.61	0.07	0.52	0.08
0.21	0.58	0.07	0.56	0.07

Table 4.4: Mean R.M.S error and standard deviation at head level

Torso level				
Radius [m]	***3.6GHz***		***19GHz***	
	Mean RMSE	***Standard Deviation***	***Mean RMSE***	***Standard Deviation***
0.15	0.54	0.05	0.49	0.09
0.20	0.56	0.06	0.54	0.11
0.25	0.53	0.08	0.52	0.11
0.30	0.48	0.05	0.52	0.11

Table 4.5: Mean R.M.S error and standard deviation at Torso level

Leg level				
Radius [m]	***3.6GHz***		***19GHz***	
	Mean RMSE	***Standard Deviation***	***Mean RMSE***	***Standard Deviation***
0.10	0.43	0.05	0.47	0.06
0.15	0.52	0.05	0.46	0.06
0.20	0.54	0.05	0.51	0.08
0.25	0.50	0.06	0.49	0.08

Table 4.6: Mean RMSE and standard deviation at leg level

5 Evaluation

5.1 Conclusion

Comparative deterministic modelling of height-dependent human-radio interaction was performed at center frequency 3.6GHz and 19GHz with 2GHz bandwidth. The channel measurement with both transmitting and receiving antennas directed towards the human body center was performed at head, torso, and leg heights of the human body. The Angle of Departure and Angle of Arrival of the antennas are varied only in the azimuth domain from 0° to 180°, both the antennas are located on an observation semi-circle. For human body modelling, the Uniform Theory of diffraction solution for dielectric circular cylinder model was simulated. The height-dependent dielectric cylinder model assumes homogeneous dielectric properties.

From the measurement data analysis, it is observed that the received power from the human body at a particular Angle of Arrival varies approximately up to 10dB (excluding the angles where Line of Sight signal is dominant) for different Angle of Departure. This indicates that the human body is not uniform and symmetric unlike cylinder wherein the power level variation is less than 3dB(excluding the angles where Line of Sight signal is dominant). There is a gradual decrease of human body attenuation averaged over Angle of Departure, approx.10dB to 15dB around Angle of Arrival: $0° - 40°$and $140° - 180°$. This could be due to the influence of obstructed Line of Sight scenario wherein the Line of Sight signal is more dominating. It is observed that human body attenuation averaged over all the Angle of Arrival and Angle of Departure at 19GHz is approx. 10dB higher than the human body attenuation at 3.6GHz at the torso, leg levels, and 6dB higher at head level. The free space loss is approximately 30dB higher than the human body attenuation at all three heights at both 3.6GHz and 19GHz. This suggests that free space loss is more dominant at the chosen frequency and distance.

The simulation model was verified for examples from the textbook, the curve pattern and dynamic range are close to the results of the existing example. However, results were not the same for examples from the literature due to missing details of the antenna pattern. The RMSE between the simulation model and the cylinder measurement results is estimated and the RMSE: 0.16, 0.40, and 0.13 at Angle of Departure 0°, 90°, and 180° respectively indicates that the simulation model fits with the cylinder measurement data. The angular power spectrum of the simulation model was compared with the measured angular power spectrum of the human body at every Angle of Departure to verify the accountability of using cylinder simplification. The results of RMSE indicates a high error at Angle of Departure between 40° to 160° approximately. At these angles transmitting antenna is directed towards the side plane of the human body. This proves that the cylinder simplification suits better only at certain AoD. The best fit radius for head, torso, and leg is 0.06m, 0.30m, 0.10m at 3.6GHz and 0.11m, 0.15m, 0.15m at 19GHz respectively.

5.2 Recommendations

- UTD dielectric cylinder simulation model is used for geometric approximation. The variation of the dielectric parameter was not influencing the results significantly. In general, the simulation model is not suitable for dielectric parameterization.
- The high RMSE at Angle of Departure $40° - 160°$ proves that cylinder simplification is not suitable at these angles. I recommend investigating if the elliptical cylinder is more suitable than a circular cylinder at these angles.
- The reason for higher attenuation at leg level compared to the torso and head level can be investigated further.

6 Future Work

- The manual positioning and the orientation of the antennas may introduce unavoidable errors, to avoid this, automatic positioning of the antennas is preferred.
- A more general parameterization, including both geometrical and dielectric information, based on the measurements on multiple humans needs to be performed.
- Elliptical cylinder geometrical approximation of the human body can be verified as a human body is more similar to an ellipsoid than a cylinder by visual inspection.
- The UTD formulation for the infinite length cylinder is considered for simulation. Since each cylinder is modelled separately the present analysis should not be influenced. The 3 joint cylinders are not modelled as a whole. For the future, I recommend considering the finite length, of the human body in the simulation. Due to the finite length there could also be edge diffraction at the top or bottom of the human body which also needs to be considered.
- The dielectric properties of the clothing and the layers of the skin can be considered in the future which further requires to include the higher-order physical mechanisms such as multiple reflections and volume scattering, etc.

References

[1] Ł. Januszkiewicz, "Model for ray-based utd simulations of the human body shadowing effect in 5g wireless systems," *International Journal of Antennas and Propagation*, vol. 2018, 2018. 1, 2

[2] Y. M.Yokota, Ikegamai and T. Fujii, "Numerical examination of em wave shadowing by human body," *Wireless System Research Center, Softbank Mobile Corp. Tokyo, Japan.* 1

[3] Y. Huang, A. Charbonneau, L. Talbi, and T. A. Denidni, "Effect of human body upon line-of-sight indoor radio propagation," in *2006 Canadian Conference on Electrical and Computer Engineering.* IEEE, 2006, pp. 1775–1778. v, 1, 2, 7

[4] Y. M.Yokota, Ikegamai and T. Fujii, "Numerical examination of em wave shadowing by human bodies between transmitter and receiver," *Wireless System Research Center, Softbank Mobile Corp. Tokyo, Japan.* 1, 3

[5] F. Mokhtari-Koushyar, M. Alamdar, and M. Fakharzadeh, "Human body scattering modeling and measurement for millimeter-wave and 5g bands," in *2019 IEEE Texas Symposium on Wireless and Microwave Circuits and Systems (WMCS).* IEEE, 2019, pp. 1–5. 1

[6] M. Ghaddar, L. Talbi, T. Denidni, and A. Charbonneau, "Modeling human body effects for indoor radio channel using utd," in *Canadian Conference on Electrical and Computer Engineering 2004 (IEEE Cat. No. 04CH37513)*, vol. 3. IEEE, 2004, pp. 1357–1360. 1, 2

[7] E. Plouhinec and B. Uguen, "Utd human body models comparison based on dual motion capture and radio measurements," in *2019 IEEE-APS Topical Conference on Antennas and Propagation in Wireless Communications (APWC).* IEEE, 2019, pp. 192–197. 1

[8] A. D. C. de Queiroz and L. C. Trintinália, "An analysis of human body shadowing models for ray-tracing radio channel characterization," in *2015 SBMO/IEEE MTT-S International Microwave and Optoelectronics Conference (IMOC).* IEEE, 2015, pp. 1–5. 2

[9] E. Plouhinec, B. Uguen, M. Mhedhbi, and S. Avrillon, "3d utd modeling of a measured antenna disturbed by a dielectric circular cylinder in wban context," in *2014 IEEE 79th Vehicular Technology Conference (VTC Spring).* IEEE, 2014, pp. 1–5. 2, 13, 16, 30, 31

[10] C. C. Johnson and A. W. Guy, "Nonionizing electromagnetic wave effects in biological materials and systems," *Proceedings of the IEEE*, vol. 60, no. 6, pp. 692–718, 1972. 3, 8

[11] Q. Wang, X. Zhao, S. Li, M. Wang, S. Sun, and W. Hong, “Attenuation by a human body and trees as well as material penetration loss in 26 and 39 ghz millimeter wave bands,” *International Journal of Antennas and Propagation*, vol. 2017, 2017. 3

[12] M. Cheffena, “Time-varying on-body wireless channel model during walking,” *EURASIP Journal on Wireless Communications and Networking*, vol. 2014, no. 1, p. 29, 2014. 3

[13] M. Fakharzadeh, J. Ahmadi-Shokouh, B. Biglarbegian, M. Nezhad-Ahmadi, and S. Safavi-Naeini, “The effect of human body on indoor radio wave propagation at 57–64 ghz,” in *2009 IEEE Antennas and Propagation Society International Symposium*. IEEE, 2009, pp. 1–4. 4

[14] J. S. Romero-Peña and N. Cardona, “Applicability limits of simplified human blockage models at 5g mm-wave frequencies,” in *2019 13th European Conference on Antennas and Propagation (EuCAP)*. IEEE, 2019, pp. 1–5. 4

[15] S. Ali and M. J. Mughal, “Narrowband characterization of the 60 ghz indoor radio channel in the presence of human bodies,” in *2010 6th International Conference on Emerging Technologies (ICET)*. IEEE, 2010, pp. 226–229. 4

[16] T. Wu, T. S. Rappaport, and C. M. Collins, “The human body and millimeter-wave wireless communication systems: Interactions and implications,” in *2015 IEEE International Conference on Communications (ICC)*. IEEE, 2015, pp. 2423–2429. 4

[17] C. Gabriel, S. Gabriel, and y. E. Corthout, “The dielectric properties of biological tissues: I. literature survey,” *Physics in medicine & biology*, vol. 41, no. 11, p. 2231, 1996. 4

[18] S. Gabriel, R. Lau, and C. Gabriel, “The dielectric properties of biological tissues: Ii. measurements in the frequency range 10 hz to 20 ghz,” *Physics in medicine & biology*, vol. 41, no. 11, p. 2251, 1996. v, 4, 18, 19

[19] S. Salman, D. Psychoudakis, and J. L. Volakis, “Determining the relative permittivity of masses in the human body,” in *Proceedings of the 2012 IEEE International Symposium on Antennas and Propagation*. IEEE, 2012, pp. 1–2. 5

[20] *UNDERSTANDING 5G SPECTRUM FREQUENCY BANDS*. 5

[21] F. Mani, “Improved ray-tracing for advanced radio propagation channel modeling,” Ph.D. dissertation, PhD Thesis, ICTEAM, UCL Belgium, 2012. 7

[22] E. Taoufik, S. Nabila, and B. Ridha, “The reflection of electromagnetic field by body tissue in the uwb frequency range,” in *2010 IEEE Radar Conference*. IEEE, 2010, pp. 1403–1407. 7

[23] D. McNamara, C. Pistorius, and J. Malherbe, "The uniform geometrical theory of diffraction," *Artech House, London*, 1990. v, v, 8, 9, 10, 14, 30

[24] J. Gutiérrez-Meana, J. Á. Martínez-Lorenzo, and F. Las-Heras, "High frequency techniques: The physical optics approximation and the modified equivalent current approximation (meca)," *Electromagnetic Wave Propagation in Complex Matter*, 2011. 8, 13

[25] P. Pathak, W. Burnside, and R. Marhefka, "A uniform gtd analysis of the diffraction of electromagnetic waves by a smooth convex surface," *IEEE Transactions on antennas and propagation*, vol. 28, no. 5, pp. 631–642, 1980. 12, 15

[26] L. Pearson, "A scheme for automatic computation of fock-type integrals," *IEEE transactions on antennas and propagation*, vol. 35, no. 10, pp. 1111–1118, 1987. 16

[27] Mathworks, *Ridge horn antenna data sheet*, https://aaronia.com/antennas/powerlog-series-horn/. 22

[28] *Rectangular horn antenna data sheet.* 22

[29] P. Series, "Effects of building materials and structures on radiowave propagation above about 100 mhz," *Recommendation ITU-R*, pp. 2040–1, 2015. 31

[30] Mathworks, *Mean*, https://nl.mathworks.com/help/matlab/ref/mean.html. 40

[31] ——, *Standard Deviation*, https://nl.mathworks.com/help/matlab/ref/std.html. 40